TAMPEREEN TEKNILLINEN YLIOPISTO
TAMPERE UNIVERSITY OF TECHNOLOGY

TUULI MIINALAINEN

NUMERICAL EEG FORWARD MODELING WITH DIPOLAR SOURCES: H(DIV) APPROACH

Master of Science Thesis

Examiners:
Asst. Prof. Sampsa Pursiainen,
Tampere University of Technology
and Prof. Dr.rer.nat. Carsten Wolters,
University of Münster
Examiner and topic approved
on 9 th August 2017

ABSTRACT

TUULI MIINALAINEN: Numerical EEG Forward Modeling with Dipolar Sources: H(div) Approach
Tampere University of Technology
Master of Science Thesis, 58 pages, 6 Appendix pages
September 2017
Master's Degree Programme in Science and Technology
Major: Mathematics
Examiners: Asst. Prof. Sampsa Pursiainen, Tampere University of Technology and Prof. Dr.rer.nat. Carsten Wolters, University of Münster, Germany
Keywords: electroencephalography, forward modeling, finite element method, source analysis, divergence conforming source model

The objective of this master's thesis project is to study forward electroencephalography (EEG) modeling with divergence conforming, finite element sources. EEG is a method for measuring electric potentials on human head, caused by neural activity in the brain. The main goals were to implement previously studied H(div) - source types to a C++ based toolbox DUNE (Distributed and Unified Numerics Environment), and also to numerically analyze the influence of the element patch size on modeling accuracy. Moreover, an adaptive version of the previously studied H(div) approach is evaluated. The numerical analysis was conducted with a spherical mesh.

The results of the numerical experiments revealed that the divergence conforming source models produce relatively accurate results near the outer gray matter layer boundary. For deeper sources that are located further away from the gray matter boundary, the reference method St. Venant gave more precise results. Moreover, the modeling accuracy for the H(div) source model improved as the size of the element patch grew. Nevertheless, for sources near the gray matter boundary, there were no significant increases in modeling precision detected after taking more than four elements in source configuration. In addition, the adaptive style did not bring any remarkable advantage to the resulting accuracy.

TIIVISTELMÄ

TUULI MIINALAINEN: Numeerinen EEG Mallinnus Dipolilähteillä: H(div)-Malli
Tampereen teknillinen yliopisto
Diplomityö, 58 sivua, 6 liitesivua
Syyskuuu 2017
Teknis-luonnontieteellinen koulutusohjelma
Pääaine: Matematiikka
Tarkastajat: Asst. Prof. Sampsa Pursiainen, Tampereen Teknillinen Yliopisto ja Prof. Dr.rer.nat. Carsten Wolters, Münsterin yliopisto, Saksa
Avainsanat: elektroenkefalografia, suora mallinnus, elementtimenetelmä, lähdeanalyysi, H(div)- lähdemalli

Diplomityön tavoitteena on toimia jatkumona aiemmille tutkimuspapereille, joissa mallinnetaan elektroenkefalografiaa H(div)-lähteillä elementtimenetelmää hyödyntäen. Elektroenkefalografia on menetelmä, jolla mitataan aivojen sähköisestä aktiivisuudesta aiheutuvaa potentiaalia pään pinnalta. Työn päämääränä oli luoda H(div)-lähdemalli C++ pohjaiseen DUNE (Distributed and Unified Numerics Environment) - ohjelmistopakettiin, ja samalla arvioida lähde-elementtien lukumäärän vaikutusta mallintamistarkkuuteen pallomaisessa verkossa. Lisäksi työssä tutkittiin adaptiivista tapaa muodostaa lähdekonfiguraatio.

Numeerisen analyysin tuloksista nähtiin, että H(div) - lähdemalli tuotti verrattain tarkat tulokset, kun mallinettiin dipolilähteitä harmaan aineen ulkoreunalta. Kun kyseessä olivat syvemmät lähteet kauempana ulkoreunasta, referenssimenetelmä St. Venant tuotti tarkemmat tulokset. Lisäksi mallinnuksen tarkkuus kasvoi, kun H(div) mallissa lähde-elementtien määrä lisääntyi. Kuitenkin huomattiin, että mallintaessa harmaan aineen ulkoreunalla sijaitsevia dipolilähteitä H(div) mallilla, tarkkuus ei enää parantunut neljän elementin versiosta, vaikka elementtien määrää lisättiin. Analyysin pohjalta myös paljastui, että adaptiivinen tyyli ei tuonut merkittävää etua lähdemallinnukseen pallon muotoisessa elementtiverkossa.

PREFACE

Over and above, I am highly grateful to my thesis supervisor Assistant Professor Sampsa Pursiainen, who has put a lot of effort and thought into this thesis project. Likewise, many thanks to my second supervisor Prof. Dr. rer. nat. Carsten Wolters at the Institute for Biomagnetism and Biosignalanalysis at the University of Münster in Germany for all the guidance and hosting me as a visiting research assistant. Similarly, I thank professor Christian Engwer from the Faculty of Mathematics and Computer Science at the University of Münster for mathematical input.

As the thesis project was carried out in co-operation with the SIM-Neuro research group at IBB, I am deeply thankful to the SIM-Neuro team members for all the help and shared ideas. Equally, the assistance by the Inverse Group members in the Department of Mathematics at TUT was highly precious. This master thesis project was supported by the Academy of Finland Key project (project 305055) and Academy of Finland Center of Excellence in Inverse Problems Research and I am much indebted to both institutes. Likewise, I would like to thank Student Affair Officer Mira Kauppinen for arraging me the ERAMUS+ grant for my master's thesis exchange period.

In addition to studying, I have enjoyed my time at TUT by participating in great student activities. I thank the guild Hiukkanen, student union TTYY, labour organisation TEK, and theater group NääsPeksi for all the unforgettable moments and for making me a true Teekkari.

Finally, I state the highest gratefulness towards my parents and siblings who have veritably supported me throughout my study path. Also, thank you Janne for lighting up my days.

Tampere, 11.08.2017

Tuuli Miinalainen

CONTENTS

LIST OF FIGURES

LIST OF TABLES

LIST OF ABBREVIATIONS AND SYMBOLS

Literal abbreviations

CSF	Cerebrospinal fluid layer
DUNE	the Distributed and Unified Numerics Environment
EW	Edgewise
EEG	Electroencephalography
e.g.	*exempli gratia*, For example
FI	Face intersecting
FEM	Finite element method
i.e.	*id est*, In other words
lnMAG	Logarithmic magnitude measure
MEG	Magnetoencephalography
PBO	Position based optimization
PSP	Postsynaptic potential
PCG	Preconditioned conjugate gradient
RDM	Relative difference measure
RT	Raviart-Thomas
SSOR	Symmetric successive overrelaxation
IQR	Interquartile range

Mathematical expressions

$\vec{v}$	Vector
$\vec{x}^T$	Transpose of a vector
$\vec{n}$	Normal vector
$\times$	Cross product
$\nabla\times$	Curl operator
div	Divergence
$\cdot$	Inner product
Δ	Laplace-operator
∇	Nabla operator
$\|\|\|_p$	p-norm
Ω	Open set in $\mathbb{R}^n$, here the head domain
$H^m(\Omega)$	Hilbert space
$RT_k(T)$	k-th order Raviart-Thomas space

$H(\text{div})$	Sobolev - Space with all functions having divergence in L^2
$\vec{w}$	Basis function in H(div)
ψ	Linear nodal basis function in $H^1(\Omega)$
δ	Dirac delta distribution
$\mathcal{T}_h(\Omega)$	Tetrahedralization of domain Ω

Electromagnetic terms

σ	Conductivity tensor
$\vec{E}$	Electric field
$\vec{B}$	Magnetic field
$\vec{J}$	Total current field
$\vec{J}^P$	Primary current field
u	Potential function
$\vec{p}$	Dipole moment
$\vec{r}$	Dipole position
$\vec{r}_{\vec{w}}$	Position of a dipolar source
$\vec{q}_{\vec{w}}$	Moment of a dipolar source

1. INTRODUCTION

This thesis project is dedicated to discovering how the divergence conforming dipolar source type is suited for modeling the neural activity in the brain. As a continuation of previous finite element method based electroencephalography studies, the intention is to implement the H(div) -type source model to a C++ toolbox called DUNE. Additionally, the objective of this study is to assess how the amount of source elements affects the modeling results.

Electroencephalography (EEG) is one of the oldest and the most used methods for detecting the neurological activity of the brain.[21, 42, 19] Measuring the electric potential differences from the surface of the head, EEG captures the dynamics of the electrical activity of neuron populations. This electrical activity is caused by the ionic currents that are generated by cellular level biochemical sources. These currents can be detected from the electric and magnetic fields that the ionic currents form. Moreover, these fields can be modeled by the laws of physics, with the help of advanced and numerical mathematics. [2]

The roots of EEG research lie in the late 19th century, when physicists investigated electrical brain activity of animals. However, the first measurements of the electric fields of the human brain were recorded in 1924 by a German psychiatrist, Hans Berger.[23, 13] As the techniques for measuring EEG signals developed during the 20th century, the mathematical applications related to biomedical imaging evolved as well. For instance, Geselowitz during the 1960's and the 1970's [28, 29] and Sarvas during the 1980's [47] were among the first ones to formulate the detailed derivation of EEG and magnetoencephalography (MEG) models, with a spherical head model and actual computer programmed methods. Later on, a numerical method known as the boundary element method (BEM) made its entrance to the field of modeling EEG source currents.[32, 19] Becoming more and more popular in 1990's, nowadays commonly used BEM is known to be computationally and memory wise relatively efficient. However, with BEM there is an assumption of a layerwise constant conductivity, lacking the three dimensional fine structures of the brain. This means that the direction dependency of the tissue conductivity in the brain cannot be included in the model. Moreover, if the distinction of the tissue

structures, such as skull compacta or the surface of the brain, is taken into account in the BEM modeling, the computational complexity and memory demand might increase significantly [35].

In recent years, researchers around the globe have started to consider the finite element method (FEM) as a sufficient method for EEG modeling. [14, 56, 37, 53] FEM enables designing a highly precise model of the head, covering also the internal folded surfaces. Furthermore, the three dimensional conductivity structure with different layers, e.g. skull compacta or spongiosa, can be taken into account within FEM modeling, with respect of anisotropic (i.e. direction depended) conductivity properties.[51] FEM provides also a base for modeling both surface and volumetric elements precisely. [46] As the research among FEM applications in EEG modeling has increased in the 2000's [25], it has been harnessed also to commercial applications, by Compumedics Neuroscan [3] and to BESA MRI 2.0 by BESA GmbH[30], for instance.

Among EEG modeling, there are two main approaches: the forward model and the inverse model. In the forward case, the aim is to compute the electrode voltages on the head surface knowing the fixed source currents and both the geometry, and internal conductivity distribution of the head. Vice versa, the inverse approach focuses on creating a reconstruction of the original source currents, based on the voltages measured on the head surface. In fact, the methods for solving the inverse problem are based on the solutions that are found via forward modeling. Although the theorems of the forward model are already rather advanced, there exist several unresolved questions related to the accuracy and efficiency that require further research.[37]

In this thesis, the focus is on the forward model, and in particular on the divergence conforming dipolar sources for EEG modeling. These source models are based on mathematically rigorous ground, on which modeling the current field is done with the divergence conforming, Raviart - Thomas (RT) basis functions. [5, 18] The source currents are modeled with mathematical point dipoles, and the positions and the strengths of the dipoles are defined between adjacent FE mesh elements and nodes. As shown in previous studies [46, 50, 12], the divergence conforming source models give as accurate or even better results as for example the classical monopolar approaches: Partial integration [55], and St. Venant method [20, 37]. In this paper, there are two types of divergence conforming sources utilized: Linear RT-basis functions that correspond to the face intersecting (FI) source dipoles and quadratic ones that formulate the edgewise (EW) sources. Both types are applied in source configurations with varying element patch size. By comparing the source configura-

tions with $1, 2, \ldots, 6$ elements in a source element patch, the impact of the patch size on model accuracy is investigated. Furthermore, the previously presented restricted dipolar source model is compared to an adaptive composition of the dipole combinations. This is done to evaluate whether the adaptability brings any improvement to the forward solution.

In addition, the aim of this thesis project is to implement the divergence conforming sources for EEG forward model in the open source software DUNE (Distributed and unified Numerics Environment). [17, 15, 10, 9] As a modular toolbox, DUNE provides a base for computing partial differential equation, including grid-based methods such as FEM. The implementation itself is done with duneuro, which is a DUNE based toolbox for solving forward EEG and MEG problems.[1, 26, 45] The source models are tested numerically with a spherical grid, and evaluated against an analytical solution with error estimates for both potential topography and magnitude aspects.

The paper is structured as follows: The principles and the neurological background of the forward EEG modeling are presented in Chapter 2. Further on, the finite element application of the forward EEG model is presented in Chapter 3 and the DUNE implementation including implementation procedure and parameters in Chapter 4. After that, the results of the numerical experiments are presented and analyzed in Chapter 5. Finally, the main conclusions are summed up together in Chapter 6.

2. EEG FORWARD MODEL

Electroencephalography (EEG) is a method for measuring potential differences that are recorded from the head surface.[2] The principles of the EEG forward modeling are presented in this chapter.

2.1 EEG

EEG is an electro-physiological method for detecting brain activity. Recording voltages from the two sites of the brain as a function of the time, it works as a graphic display for neural activity in brain cells. [48, 19] The great advantage of EEG is that it is noninvasive, meaning that the brain activity is measured only from outside of the head. With EEG, the activity can be measured in a millisecond range. Therefore, as an electrical event related to a single neuron lasts from one to tens of milliseconds, EEG enables the detection of rapid changes in neural activity, that further on reveal the signal processing in the brain. [33] One development point of EEG modeling is detecting the source of neural activity as precisely, or in biomedical terms, as focal as possible. [53]

In addition to EEG, magnetoencephalography (MEG) is also a commonly used imaging technology. When measuring magnetic fields induced by electrical currents in the nerves, MEG produce relatively precise results in respect of timing. [24, 19] However, as the magnetic fields in the human head are extremely weak and measuring them requires highly sensitive instruments, the MEG systems are remarkably expensive. On the contrary, the electrical currents are notably easier to measure and that is why EEG infrastructure does not require as great investments as MEG. [43] Also, EEG reveals both radial and tangential sources while MEG shows only tangential ones, but those with a much higher spatial accuracy.[19] Therefore, MEG and EEG are typically measured simultaneously. [24, 8, 7]

2.2 Neurological Background

The central neural system consists of nerve cells and glia cells. The body of the nerve cell is called a *soma*, and "the junction area" of two nerve cells *synapses*. In addition to soma, synapses cover also *an axon hillock* and dendrities. *Axons* and *dendrites* are contact channels to other cells or organs, axons being the ones to export signals and dendrites the ones to import them into the neuron. One dendrite can consist of several thousands of branches, and a single branch is able to receive a signal from other cells. In contrast, an axon is typically a single branch, transmitting the output signal to other parts of the nervous systems. In general, the length of an axon can vary from less than a millimeter to over a meter, whereas a dendrite is usually approximately two millimeters long. [48] There exist several thousand synapses covering nerve cells. The glia cells are embedded somas, dendrites, and axons, and they contact somas and operate on other processes of the nerve cells. [2]. The structure of a nerve cell is presented in Figure 2.1.

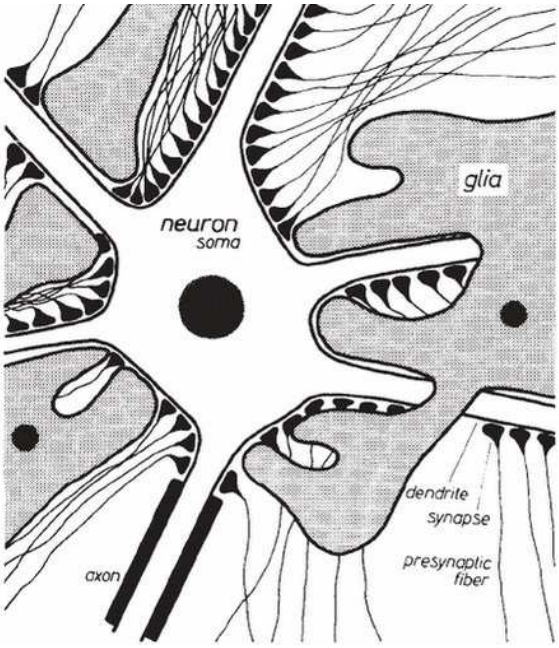

Figure 2.1 *A schematic drawing of the neuronal and glial parts of a nerve cell [49]*

2.2.1 Neural Activity in the Brain

The electrical impulses that neurons fire are called action potentials. The neuron collects intracellular potential through the excitatory synapses, transferred in by dendrites. This collection is also known as summation. If there is only one axon continuously bringing potentials to the receiving neuron, this is referred as temporal

summation. In turn, if there is more than one axon firing at the same time to one neuron, this event is called spatial summation. Finally, the receiving neuron fires an action potential as soon as the potential level at the axon hillock has reached a specific threshold level.

A neuron is surrounded by a ten nanometers thick membrane, dividing the tissue into intracellular and extracellular elements that differ in ion concentrations. There are special protein molecules on the membrane that control the concentration difference and pump certain ions against the concentration gradient. As the action potential changes the permeability of the ions, the voltage across the membrane changes as well.[33]

The electrical potentials enter a cell via ion channels. At first, an electric pulse travels along the presynaptic cell's axon. Certain transmitter molecules from the synaptic vesicles into the synaptic cleft at the same time. Some of the molecules diffuse fast through the gap, while others attach themselves to receptors on the postsynaptic cell's surface. This modifies the shape of the receptor molecules and result in the ion channels opening through the membrane. Subsequently, the open ion channels enable ions, mostly Sodium Na^+, Potassium K^+, and Chlorine Cl^- ions to flow and change the membrane potential in the receiving cell. This occasion is known as the postsynaptic potential (PSP). [33]

Postsynaptic Potentials

As the transmitter molecules reach the postsynaptic cell, there is a change in the membrane's permeability for certain ions. Furthermore, the potential on the membrane surface and surroundings alters. This produces an electric field and a current throughout the interior of the postsynaptic cell. Further, the resulting current has two options: Either it flows out if the channels for potassium or chloride are activated and the cell is inhibited. Alternatively, the current can flow into the cell in case if sodium channels are open, and there exists an excitatory PSP. The typical voltage over the membrane is approximately $\Delta V = 25$ millivolts, and the current $W = 20$ femtoamperes for a single PSP. [33]

Action Potentials

The signal transfer along an axon depends on how the membrane is able to change its permeability for Na^+ and K^+ ions, which occurs when the approaching action

potential makes the voltage-sensitive channels open themselves. As mentioned previously, the launch of an action potential necessitates that the voltage at the axon hillock exceeds the threshold voltage, typically roughly 40 millivolts. During this event, the interior of the cell is positive charged for a short period. As a result, this potential change has an effect to the surrounding region, which allows the action potential to travel along the axon with undiminished amplitude. If the excitatory input becomes stronger, it only increases the frequency of firing, whereas the amplitude of the action potentials remain at the same level. [33] The action potential can be estimated by current dipoles that are oriented oppositely and therefore forming a current quadrupole. [33]

Capturing the Neural Activity with EEG

In the light of that measuring outside of the head requires the current dipole moments to be on the order of 10 nanoampere meters, it becomes clear that there must be roughly a million synapses active for a measurable evoked response. Nevertheless, since the brain surface consists of 10^5 pyramidal cells per a square millimeter, and a neuron has thousands of synapses, the simultaneous activation of one synapse in a thousand over an area of one square millimeter would theoretically be enough to produce a measurable signal. Virtually, a detectable signal requires activation of larger areas due to the cancellation effect by the currents from opposite directions. [33]

Although the strength of an action potential is much greater than for a PSP, the signals detected in the far field (on the surface of the head) are mostly from the PSPs. This is due to the fact that the PSP event goes on longer than an action potential. As mentioned in the previous paragraph, there are cancellation effects among the cell currents caused by the potentials from opposite directions. Therefore, the dominant current component is the one that is flowing towards the postsynaptic cell's body, in other words by PSP. This means that the sources for EEG are current dipoles. [25]

2.2.2 The Structure of the Brain

The human brain can be divided into three primary elements: brainstem, cerebellum, and cerebrum, shown in Figure 2.2.

The brainstem works as a stalk of the brain, and is a channel for nerve fibers for transferring signals between higher brain centers and the spinal cord.

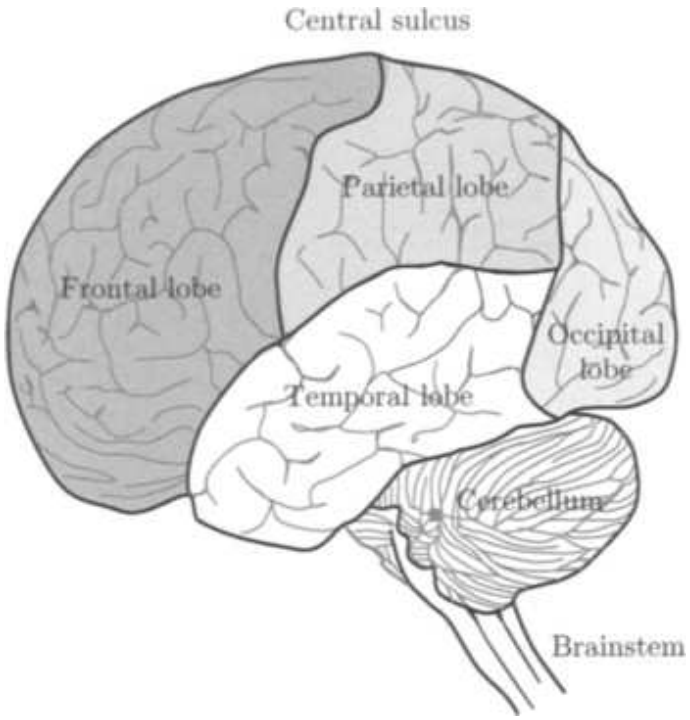

Figure 2.2 *The structure of a human brain [48]*

The thalamus is located in the middle of the cerebrum, and it functions as a relay station. The cerebellum is a tiny part in the back of the human head, which controls fine muscle movements. The cerebrum itself is divided into two halves. [44] The outer area of the cerebrum is called the cerebral cortex, and has an altogether surface area of approximately 1600 centimeters. The thickness of the cerebral cortex is between two to three millimeters, and it contains roughly 10^{10} neurons. [33] The cortex is also called *gray matter*. Right below the gray matter is the *white matter* area. [44] As shown later on in Figure 3.1, the brain is surrounded by the cerebrospinal fluid layer (CSF), which is again covered by skull and further on with scalp. In fact, the skull layer consists of two layers: an outer compartment compacta, and an inner one, spongiosa. Moreover, the brain is divided by a longitudinal fissure into two hemispheres, generally known as the left and right halves. These halves are divided further on into four lobes: frontal, parital, temporal, and occipital. [33]

2.2.3 Measuring and Modeling Neural Activity

The electrical activity of the brain can be divided into three subcategories: The first one is spontaneous potentials, e.g. alpha and sleep rhythms. The second type of the activity is evoked or event related potentials, usually as the response for some stimulus. The last type is potentials generated by a single neuron and recorded by

microelectrodes. [44]

If the primary source and the distribution for surrounding connectivity are determined, the resulting electric potentials can be computed from Maxwell's equations. Due to the linearity of the Maxwell's equations, it is sufficient to have the solution for only the elementary current dipole. Further, the fields of more complex sources can be computed easily with the superposition principle. [33, 19]

Detecting the source currents from an externally measured field by EEG is a typical inverse problem. However, it was shown already by Hermann von Helmholtz in 1853 that this problem cannot be solved uniquely. [33, 19] Moreover, the inverse solution is extremely sensitive to small changes in the measured, noisy EEG data. [31]

It is required to apply source models (i.e. current dipoles) or other selective estimation techniques for interpreting the EEG data [33] and constructing an accurate forward model, that can be harnessed for improving the inverse solutions.

2.3 Maxwell's Equations

As noted in previous wording, the resulting electric potential of neural activity can be calculated with Maxwell's equations. In the interest of simplifying the equations, there are two notable assumptions made: The first one is that the magnetic permeability of the head tissue is the same as for free space, i.e. $\mu = \mu_0$. Another assumption lies in the quasi-static approximation of the source, meaning that for a magnetic field $\vec{B}$, the term $\partial\vec{B}/\partial t$ can be dropped. Then the Maxwell's equations are of the form

$$\nabla \cdot (\epsilon \vec{E}) = \rho \tag{2.1}$$

$$\nabla \times \frac{\vec{B}}{\mu_0} - \varepsilon \frac{\partial \vec{E}}{\partial t} = \vec{J} \tag{2.2}$$

$$\nabla \cdot \vec{B} = 0 \tag{2.3}$$

$$\nabla \times \vec{E} = 0, \tag{2.4}$$

where the $\vec{J}$ is the total electric current, $\vec{E}$ the electric field, ρ the charge density and ε is the electrical permittivity. The nabla-operator $\nabla = (\frac{\partial}{\partial x}, \frac{\partial}{\partial y}, \frac{\partial}{\partial z})^T$ results in a column vector of partial derivatives. [19]

2.4 Source Currents

In the case of quasi-static approximation, it follows from the equation 2.4 that the electric field is actually the gradient of a scalar potential function $u(x)$, i.e.

$$\vec{E} = -\nabla u. \tag{2.5}$$

As the resulting electrical potentials originate from the dentritic currents, the total source current $\vec{J}$ can be split into two terms: intracellular and extracellular components. The intracellular, so-called primary component $\vec{J}^P$ corresponds to the parallel currents moving in dendrites of the activated pyramidal cell. Likewise, the extracellular component $\vec{J}_e$, known as the volume current, represents the current that returns through the extracellular space. [19] As described earlier in Section 2.2.1, the primary current $\vec{J}^P$ is the result of opened ion channels. In other words, the currents are sourced by the ion channels pumping ions out and into the cell, against the concentration gradients. [42] Moreover, as the extracellular current is a passive current, and it therefore fulfills the Ohm's law $\vec{J}_e = \sigma\vec{E}$. The total current is

$$\vec{J} = \vec{J}^P + \sigma\vec{E}, \tag{2.6}$$

in which the conductivity tensor σ is

$$\sigma = \begin{pmatrix} \sigma_{xx} & \sigma_{xy} & \sigma_{xz} \\ \sigma_{yx} & \sigma_{yy} & \sigma_{yz} \\ \sigma_{zx} & \sigma_{zy} & \sigma_{zz} \end{pmatrix}.$$

Taken into account that $\sigma_{xy} = \sigma_{yx}$ (and similarly for components y and z), the conductivity tensor can be abbreviated to

$$\sigma = \begin{pmatrix} \sigma_{xx} & \sigma_{xy} & \sigma_{xz} \\ \sigma_{zy} & \sigma_{yy} & \sigma_{zz} \end{pmatrix}.$$

For some parts of the brain (e.g. CSF), the tissue conductivity is a linear function of distance, i.e. $\sigma = \sigma(\vec{x})$, and the material is isotropic in that case. If the conductivity depends on the direction, the tissue in the brain is anisotropic and the same potential differences may result in different currents on the opposite sites of the anisotropic elements. [19]

Applying the Equation 2.5 to the divergence of the Equation 2.6, the resulting

formula is

$$\nabla \cdot \vec{J} + \nabla \cdot (\sigma \nabla u) = \nabla \cdot \vec{J}^P. \tag{2.7}$$

Since the law of the total charge conservation yields $\nabla \cdot \vec{J} = 0$ [47], the Equation 2.7 can be expressed as

$$\nabla \cdot (\sigma \nabla u) = \nabla \cdot \vec{J}^P \tag{2.8}$$

on the domain Ω, which corresponds to the area of brain that is modeled. [33, 19]

For Equation 2.8, the boundary conditions originate from the fact that the head is electrically isolated, implying that all the currents remain inside the head. In mathematical terms, the outward pointing normal vector $\vec{n}$ on a surface $\partial\Omega$ can be expressed as

$$(\sigma \nabla u) \cdot \vec{n} = 0. \tag{2.9}$$

[19]

The term 2.9 is known as the homogeneous Neumann boundary condition. [46]

2.4.1 Mathematical Dipole

The source term $\vec{J}^P$ defines the electrical activity in the brain. As mentioned previously, the source currents can be modeled as dipoles. In this case it is assumed that there are two point charges with opposite signed magnitudes Q and -Q, and that these points have a distance $\vec{d}$. This way a dipole moment can be presented as $\vec{p} = Q\vec{d}$.

However, within EEG modeling it is often assumed that the source is highly focal, focused in a single point. Setting distance $\vec{d} \to 0$ would push $Q \to \infty$ since the dipole moment $\vec{p}$ is not changing. Therefore, as the dipole is set to a single position $\vec{r}_0$, the variables Q and $\vec{d}$ are omitted and the mathematical dipole can be written as

$$\vec{J}^P = \vec{p}\delta(\vec{r} - \vec{r_0}), \tag{2.10}$$

in which δ is the Dirac delta distribution. The Equation 2.10 is a generally accepted model for the activity of the human brain. [33, 19, 42]

3. FINITE ELEMENT METHOD FOR EEG FORWARD PROBLEM

The finite element method (FEM) has become a widely used method for finding numerical solutions for several engineering problems. Typical applications vary from stress and deformation analysis of aircrafts, automotive, buildings, and bridges, as well as the field analysis of heat flow or magnetic flux. [22] Especially when it comes to solving boundary value problems for partial differential equations, FEM provides an accurate framework with a fast computational aspect. [18]

3.1 The Concept of the Finite Element Method

The first factual mathematical contribution to finite element theory is considered Courant's paper in 1943. Later on, at the end of the sixties and the beginning of the seventies, FEM became more popular and developed by engineers.[18]

The overall idea of FEM modeling is that to discretize the volume Ω into a set of smaller, discrete subdomains, and these sub regions are called elements. Within each element there are defined nodes connected by edges. In multidimensional cases, the nodes and edges assemble faces. Furthermore, the basis functions are defined over each element.[22]

The advantages of modeling head geometry with FEM lie on its grounding concept: Instead of looking for a solution for the infinite-dimensional function space where the variational problem is introduced, the aim is to find the solution for a finite-dimensional function space. Furthermore, this space is in most cases chosen as a subspace of the original function space. For creating a finite-dimensional subspace, the volume Ω is approximated with a set of basic geometrical objects, and this is known as triangulation. In a three dimensional case, the volume is usually subdivided into tetrahedra or hexahedra. In this study, the tetrahedron is chosen as the element type, since it is known to support accurate approximation of the geometrical structures of the head. [50]

A finite element (FE) mesh for a human head is presented in Figure 3.1.

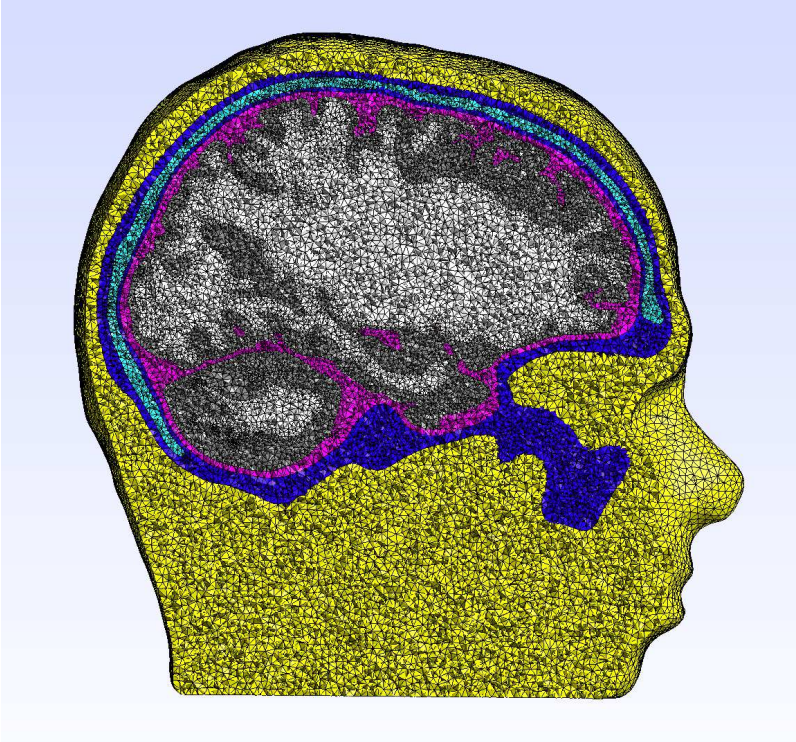

Figure 3.1 *A realistic FE mesh for a human head*

The mesh in Figure 3.1 is constructed from real measured MRI - data, provided by the IBB Institute in Münster. [51] The white matter compartment is marked with white color, gray matter with dark gray, CSF layer with purple, and skin with yellow. Also, the skull is divided into compacta (dark blue) and spongiosa (light blue). In this thesis, the mesh applied is not a realistic model, but a sphere due to the existence of an analytical solution.

3.2 Formulating the FE System

The fundamental idea of the finite element method is to find the solution for a finite-dimensional function space, in place of an infinite-dimensional one. [50] In the following section the base for the finite element system for the EEG forward problem is derived.

3.2.1 Sobolev Spaces

The Sobolev spaces are built on the function space $L_2(\Omega)$, which consists of all square-integrable functions $u(x)$ over Ω. The functions u and v are identified whenever $u(x) = v(x)$ for $x \in \Omega$, except on a set of measure zero. Now $L_2(\Omega)$ is a Hilbert

space, associated with scalar product

$$(u, v)_0 := (u, v)_{L_2} = \int_\Omega u(x)v(x)dx \tag{3.1}$$

with the norm

$$\|u\|_0 = \sqrt{(u, u)_0}. \tag{3.2}$$

Definition 3.2.1 *The function $u \in L_2(\Omega)$ holds a weak derivative $v = \partial^\alpha$ in $L_2(\Omega)$, given that $v \in L_2(\Omega)$ and*

$$(\phi, v)_0 = (-1)^{|\alpha|}(\partial^\alpha \phi, u)_0 \text{ for all } \phi \in C_0^\infty(\Omega), \tag{3.3}$$

where $C_0^\infty(\Omega)$ is a subspace of the space $C^\infty(\Omega)$ that consists of the functions that are infinitely differentiable. $C_0^\infty(\Omega)$ includes the functions of $C^\infty(\Omega)$ that are nonzero only on a compact subset of Ω.

Furthermore, if the function is differentiable in the classical sense, then it also has a weak derivative, and the actual and weak derivative match. This also means that Equation 3.3 becomes Green's formula for integration by parts. [18]

The theorem of the weak derivative holds also for other differential operators. For example, if it is denoted that $u \in L_2(\Omega)^n$ is a vector field, it results that $v \in L_2(\Omega)$ is the divergence of u in the weak sense. In other words, $v = \text{div } u$, given that $(\phi, v)_0 = -(\text{grad } \phi, u)_0$ for all $\phi \in C_0^\infty(\Omega)$. [18]

Definition 3.2.2 *Provided an integer $m \geq 0$, let the space $H^m(\Omega)$ consist of all functions $u \in L_2(\Omega)$, which have the weak derivatives $\partial^\alpha u$ for all $|\alpha| \leq m$. A scalar product on $H^m(\Omega)$ can be defined as*

$$(u, v)_m := \sum_{|\alpha| \leq m} (\partial^\alpha u, \partial^\alpha v)_0, \tag{3.4}$$

and the corresponding norm as

$$\|u\|_m := \sqrt{(u, u)_m} = \sqrt{\sum_{|\alpha| \leq m} \|\partial^\alpha u\|^2_{L_2(\Omega)}}. \tag{3.5}$$

The space $H^m(\Omega)$ is complete in respect to the norm $\|\cdot\|_{m,\Omega}$ and therefore a Hilbert space. [18]

3.2.2 Weak Formulation

Considering the continuity properties, it is a rather challenging problem to find the exact solution for Equation 2.8 that fulfills also the boundary conditions. Instead, one answer is the concept of weak formulation, where the result is a numerical approximation equipped with less binding continuity requirements. [27]

In order to solve the potential u in a weak sense, Equation 2.8 is integrated by parts and multiplied by a test function v, resulting in the weak form

$$\int_\Omega \nabla v \cdot (\sigma \nabla u) dV = -\int_\Omega v(\nabla \cdot \vec{J}^P) dV \quad \text{for all} \quad v \in H^1(\Omega), \tag{3.6}$$

in which H^1 is a Sobolev space, with all the first-order partial derivatives being square integrable. This equals that $v \in H^1$ is in $L_2(\Omega)$. [46]

3.2.3 The Discretization of the System

In this paper, the discretization (triangulation) of the mesh is formed with tetrahedra, marking $\mathcal{T}_h(\Omega)$ to be a tetrahedralization of the domain Ω. Here h denotes that the maximum diameter of each element $T \in \mathcal{T}_h$ is $2h$. It holds that

$$\Omega = \bigcup_{n=1}^{N} T_n, \tag{3.7}$$

in which N is the amount of elements in the triangulation. Furthermore, the intersections are described as

$$T_i \cap T_j = 0 \text{ or } T_i \cap T_j \text{ is a vertex, an edge or a side face of } T_i \text{ and } T_j. \tag{3.8}$$

[18]

The solution of Equation 3.6, i.e. the potential density can be approximated as

$$u_h = \sum_{i=1}^{N} z_i \psi_i, \tag{3.9}$$

in which $\psi_1, \psi_2, \ldots, \psi_N \in H^1(\Omega)$ are linear nodal basis functions. Similarly, the primary current density can be approximated as follows:

$$\vec{J}_h^P = \sum_{j=1}^{K} x_j \vec{w}_j, \tag{3.10}$$

where $\vec{w}_1, \vec{w}_2, \ldots, \vec{w}_K \in H(div)$ are the corresponding basis functions for a source model, K being the amount of elements in the discretized mesh.[46] The Equations 3.9 and 3.10 can be associated with the corresponding coordinate vectors $\mathbf{z} = (z_1, z_2, \ldots, z_N)$ and $\mathbf{x} = (x_1, x_2, \ldots, x_K)$. Taking the Equation 3.6 as a base, the linear system can be expressed as

$$\mathbf{Az} = \mathbf{Gx}, \tag{3.11}$$

in which $\mathbf{A} \in \mathbb{R}^{N \times N}$ is a stiffness matrix and each element of $\mathbf{A}$ is defined as $A_{i,j} = \int_\Omega \nabla\psi_j \cdot (\sigma\nabla\psi_i)dV$. Likewise, $\mathbf{G} \in \mathbb{R}^{N \times K}$ with $G_{i,j} = \int_\Omega \psi_i(\nabla \cdot \vec{w}_j)dV$.

If the coordinate vector $\mathbf{x}$ is provided, the corresponding coordinate vector $\mathbf{z}$ for the potential field can be computed by forming first a load vector $\mathbf{f} = \mathbf{Gx}$, and then solving the system $\mathbf{Az} = \mathbf{f}$. Here the load vector $\mathbf{f}$ denotes a model-specific right-hand side vector.[46]

Finally, an electrode voltage vector $\mathbf{y}$ can be formed in a way that it defines the measured voltages on the surface of the head at the EEG electrode locations as $\mathbf{y} = \mathbf{Rz}$. Here $\mathbf{R} \in \mathrm{R}^{L \times N}$ defines a restriction matrix that picks the values for skin potential at the electrode locations $e_1, e_2, \ldots e_L$ on the surface $\partial\Omega$. Moreover, matrix $\mathbf{R}$ also denotes the zero level for the potential. The elements for $\mathbf{R}$ are defined as follows:

1. If the ℓ-th electrode is located at the i_ℓ-th node, $R_{\ell,i_\ell} = 1 - 1/L$.
2. If $\ell \neq j$, then $R_{\ell,i_j} = -1/L$.
3. If there is no electrode associated with j-th node, $R_{\ell,j} = 0$.

[46]

Finding the vector $\mathbf{z} = \mathbf{A}^{-1}\mathbf{f}$ requires computing an inverse for the matrix $\mathbf{A}$. As the dimensions of $\mathbf{A}$ are relatively large, calculating the inverse might not be computationally efficient. [52, 50] Thus, the electrode voltage vector $\mathbf{y}$ is formulated as

$$\mathbf{y} = \mathbf{Rz} = \mathbf{RA^{-1}Gx} = \mathbf{RA^{-1}f} = \mathbf{Tf}, \tag{3.12}$$

where matrix $\mathbf{T} = \mathbf{RA^{-1}}$ is a so-called transfer matrix. [46] Now the system 3.12 can be solved efficiently with preconditioned gradient solvers, e.g. with the conjugate gradient method (CGM) method equipped with an algebraic multigrid preconditioner (AMG). [54]

After discretization, there are several possibilities how to model the load vector $\mathbf{f}$. There are options like either to apply a monopolar source model, dipolar source model or a hybrid of these two. In following chapter, different approaches for finding $\mathbf{f}$ are presented.

3.3 The H(div)- Approach

The motivation for the dipolar approach rises from the aim to find a robust model with focal sources. Therefore, it is rational to investigate vector-valued functions, in a way that the term $\nabla \cdot \vec{J}^P$ is well-defined and square integrable, i.e $\nabla \cdot \vec{J}^P \in L^2(\Omega)$. [50] In this thesis, there are two types of dipolar sources utilized: the face intersecting (FI) and edgewise (EW) source dipoles. Both of them are formulated via Raviart-Thomas basis functions, linear ones corresponding to the FI and quadratic functions corresponding to the EW sources. Moreover, both types fall into the category of Nédélec's basis functions.[46]

3.3.1 H(div)-Space and Raviart-Thomas Elements

Whitney (Raviart-Thomas) basis functions are a suitable choice for modeling finitely supported source currents, since they are the simplest piecewise first-order polynomials.[12] Like required in Equation 2.9, the Whitney functions fulfill the boundary condition with a continuous vector field normal component over the element faces. [50]

The space $H(\mathrm{div};\Omega)$ is defined as follows:

Definition 3.3.1 *The space $H(div;\Omega)$ is defined as*

$$H(div;\Omega) := \{\mathbf{q} \in L^2(\Omega)^3 | \nabla \cdot \mathbf{q} \in L^2(\Omega)\} \tag{3.13}$$

Approximating $H(\mathrm{div};\Omega)$ as a discrete case, the space can be chosen to be RT_0, the lowest-order Raviart-Thomas elements. The advantage of the RT-elements is that the normal component is defined to be continuous on element boundaries. Therefore, the RT-elements conform in $H(\mathrm{div};\Omega)$. [50]

The discrete space V_h is formed via the space of polynomials. [50] Denoting d as the dimension of Ω, P_k can be set to be the space of polynomials in d variables of

degree $p \leq k$. Similarly, the space of homogeneous polynomials of degree k to $\tilde{P}_k$ by

$$P_k(T) := \text{span}\{\prod_{i=1}^{d} {x_i}^{\alpha_i} : \mathbf{x} \in T, \alpha \in \mathbb{N}^d, \sum \alpha_i \leq k\} \tag{3.14}$$

$$\tilde{P}_k(T) := \text{span}\{\prod_{i=1}^{d} {x_i}^{\alpha_i} : \mathbf{x} \in T, \alpha \in \mathbb{N}^d, \sum \alpha_i = k\}. \tag{3.15}$$

Subsequently, the Raviart-Thomas elements are built with these spaces as follows:

Definition 3.3.2 *For tetrahedralization $\mathcal{T}(\Omega)$, the k-th order Raviart-Thomas elements are defined on each element $T \in \mathcal{T}_h$ as*

$$\begin{aligned} RT_k(T) :&= (P_k(T))^d + \mathbf{x}\tilde{P}_k(T), \\ RT_k(\mathcal{T}_h) :&= \{\mathbf{q} \in L^2(\Omega)^3 : \mathbf{q}|_T \in RT_k(t) and < \mathbf{q}, \mathbf{n} > \textit{ is cont. over } \partial T \ , \forall T \in \mathcal{T}_h\} \\ &= \{\mathbf{q} \in L^2(\Omega)^3 : \mathbf{q}|_T \in RT_k(t) \textit{ for all } T \in \mathcal{T}_h\} \cap H(div; \Omega). [18] \end{aligned} \tag{3.16}$$

Now the potential u can be solved from Equation 3.6 if the primary current density has a square integrable divergence. In other words, if $\vec{J}^P \in H(\text{div}) = \{\vec{w} | \nabla \cdot \vec{w} \in L^2(\Omega)\}$. [46]

3.3.2 Transformation from Local to Global Mesh

The discretized mesh is constructed by mapping local reference basis functions $\hat{\phi}$ to the global mesh. Assuming a reference tetrahedron $\hat{T}$, every element $T \in \mathcal{T}_h$ is an image of the reference with a smooth bijective mapping $\mathbf{F_T}$, and the Jacobian of this mapping can be denoted by $\mathbf{J_T}$. [5]

Having the local basis function $\hat{\phi}$ that is defined on the reference element $\hat{T}$, a global basis function ϕ for H(div) can be formed. This is defined on a physical element $T \in \mathcal{T}_h$. This is done via the contravariant Piola transformation, defined as

$$\phi_{|T} = \frac{1}{det(\mathbf{J_T})}(\mathbf{J_t}\hat{\phi}) \cdot {\mathbf{F_T}}^{-1}. \tag{3.17}$$

Also, the Piola transformation is known to have the crucial property

$$\frac{1}{det(\mathbf{J_T})}\mathbf{J_T}(\hat{\delta}\hat{\lambda_0} \wedge \hat{\delta}\hat{\lambda_i}) = \delta\lambda_0 \wedge \delta\lambda_i. \tag{3.18}$$

[5]

Further along this thesis, the basis functions presented are all in global mesh form.

3.3.3 Linear RT Basis Functions

The linear basis functions correspond to the lowest order Raviart-Thomas space. Following from the Definition 3.3.2, with the lowest order $k = 0$, the space $RT_0(T)$ is defined as

$$RT_0(T) := \{\mathbf{a} + b\mathbf{x} : a \in \mathbb{R}^3, b \in \mathbb{R}, x \in T\} \subset H(\mathrm{div}, T). \tag{3.19}$$

[50]

The linear and the quadratic basis functions are visualized in Figure 3.2.

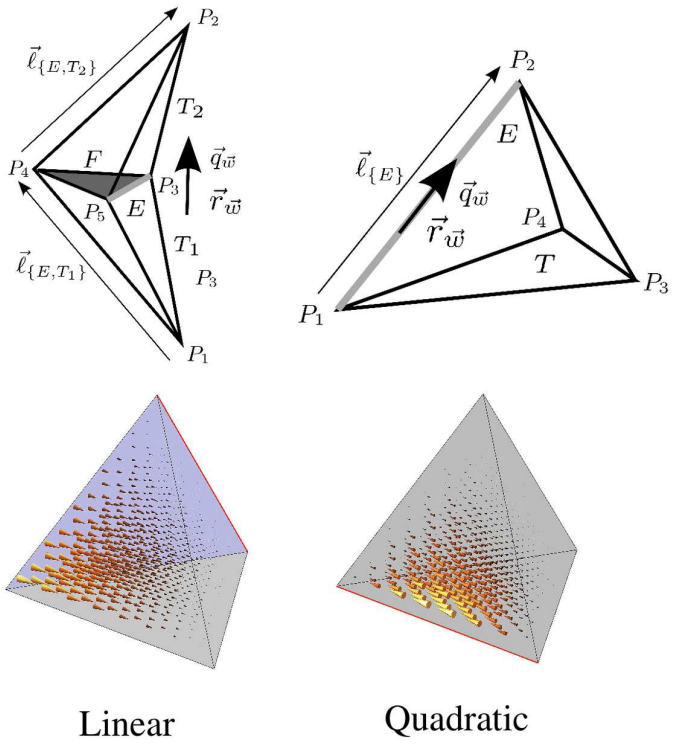

***Figure** 3.2 Tetrahedra for both linear (face intersecting) and quadratic (edgewise) basis functions. The resulting synthetic dipole is marked with an arrow. [46]*

The linear RT_0 - function is face-based, meaning that it is supported in two adjacent tetrahedra T_1 and T_2, as shown in Figure 3.2. The common face of tetrahedra is $F = T_1 \cup T_2$. The basis of RT_0 is defined by the functions in a way that the normal

derivative is zero on all faces except on the shared face F, where the derivative is continuous across the face. [50]

The basis functions for a reference element RT_0 space can be defined as

$$\vec{w}(\vec{r}) = \begin{cases} \frac{|F|}{3V_{T_1}} \frac{r\vec{P}_2 - \vec{r}}{\|r\vec{P}_2 - r\vec{P}_1\|_2} & \text{if } \vec{r} \in T_1, \\ \frac{|F|}{3V_{T_2}} \frac{\vec{r} - r\vec{P}_2}{\|r\vec{P}_2 - r\vec{P}_1\|_2} & \text{if } \vec{r} \in T_2, \\ 0 & \text{otherwise.} \end{cases} \tag{3.20}$$

Here $|F|$ is the area of a face F and V_T the volume of T.

For a single tetrahedron T, a basis function is of the form

$$\vec{w}_{\{E,F,T\}} = c_{\{E,F\}} \psi_{\{F,T\}} \frac{\vec{\ell}_{\{E,T\}}}{V_T}, \tag{3.21}$$

where E is an edge, $\vec{\ell}_{\{E,T\}}$ an edge vector, and $\psi_{\{F,T\}}$ is the linear nodal basis function for T, associated with the node opposite to F. It holds that for any linear nodal basis function ψ, the integral is $\int_T \psi = V_T/4$. [46]

The dipolar moment describes the magnitude of the source current. The dipolar moment is composed from the basis function $\vec{w}$ as

$$\vec{q}_{\vec{w}} = \int_\Omega \vec{w}\, dV, \tag{3.22}$$

and since $\vec{w}$ was associated with both T_1 and T_2, Equation 3.22 can be formulated as

$$\begin{aligned} \vec{q}_{\vec{w}} &= \textstyle\int_{T_1} \vec{w}_{\{E,F,T_1\}} dV + \int_{T_2} \vec{w}_{\{E,F,T_2\}}\, dV \\ &= c_{\{E,F\}} \frac{\vec{\ell}_{\{E,T_1\}}}{V_{T_1}} \int_{T_1} \psi_{\{F,T_1\}}\, dV + c_{\{E,F\}} \frac{\vec{\ell}_{\{E,T_2\}}}{V_{T_2}} \int_{T_2} \psi_{\{F,T_2\}}\, dV, \end{aligned} \tag{3.23}$$

yielding

$$\vec{q}_{\vec{w}} = c_{\{E,F\}} \frac{\vec{\ell}_{\{E,T_1\}}}{V_{T_1}} \frac{V_{T_1}}{4} + c_{\{E,F\}} \frac{\vec{\ell}_{\{E,T_2\}}}{V_{T_2}} \frac{V_{T_2}}{4}. \tag{3.24}$$

If $c_{\{E,F\}}$ is defined by edge vectors $\vec{\ell}_{\{E,T\}}$ as

$$c_{\{E,F\}} = \frac{4}{\|\vec{\ell}_{\{E,T_1\}} + \vec{\ell}_{\{E,T_2\}}\|}, \tag{3.25}$$

and moreover, writing with position vectors $\vec{r}_{P_i}$

$$c_{\{E,F\}} = \frac{4}{\|\vec{r}_{P_2} - \vec{r}_{P_1}\|}. \tag{3.26}$$

Next the dipole moment in Equation 3.24 can be written as

$$\vec{q}_{\vec{w}} = \frac{\vec{\ell}_{\{E,T_1\}} + \vec{\ell}_{\{E,T_2\}}}{\|\vec{\ell}_{\{E,T_1\}} + \vec{\ell}_{\{E,T_2\}}\|} = \frac{\vec{r}_{P_2} - \vec{r}_{P_1}}{\|\vec{r}_{P_2} - \vec{r}_{P_1}\|}. \tag{3.27}$$

[46]

The position $\vec{r}_{\vec{w}}$ of the dipolar source can be formulated in several ways as a function of the positions of the nodes P_i and P_j. Bauer *et al.* [12] have shown that an intuitive choice for the dipole position is the middle of these two nodes that share a face:

$$\vec{r}_{\vec{w}} = \frac{1}{2}(\vec{r}_{P_i} + \vec{r}_{P_j}). \tag{3.28}$$

Remembering that if the basis function is linear, basis function $\psi_{\{F,T\}}$ increases from 0 to 1 following a path that corresponds to vector $\vec{\ell}_{\{E,T\}}$. This results that $\nabla\psi_{\{F,T_2\}} \cdot \vec{\ell}_{\{E,T_2\}} = -\nabla\psi_{\{F,T_1\}} \cdot \vec{\ell}_{\{E,T_1\}} = 1$. Therefore, the right hand side matrix G grows into

$$\begin{aligned} G_{\{\psi,\vec{w}\}} &= -\int_\Omega (\nabla \cdot \vec{w})\psi \, dV \\ &= -c_{\{E,F\}}\nabla\psi_{\{F,T_2\}} \cdot \frac{\ell_{\{E,T_2\}}}{V_{T_2}} \int_{T_2} \psi \, dV \\ &\quad -c_{\{E,F\}}\nabla\psi_{\{F,T_1\}} \cdot \frac{\ell_{\{E,T_1\}}}{V_{T_1}} \int_{T_1} \psi \, dV \\ &= \frac{s_{\{\psi,P_2\}} - s_{\{\psi,P_1\}}}{\|\vec{\ell}_{\{E,T_2\}} + \vec{\ell}_{\{E,T_1\}}\|} = \frac{s_{\{\psi,P_2\}} - s_{\{\psi,P_1\}}}{\|\vec{r}_{P_2} - \vec{r}_{P_1}\|}, \end{aligned} \tag{3.29}$$

in which

$$s_{\{\psi,P\}} = \begin{cases} 1 & \text{if } \psi \text{ is the corresponding function for node } P, \\ 0 & \text{otherwise.} \end{cases} \text{.[46]} \tag{3.30}$$

3.3.4 Quadratic Basis Functions

The piecewise linear subspace can be complemented into a quadratic subspace with the edge-based interior functions. Each basis function is supported on the set of n tetrahedra $T_1, T_2, \ldots, T_n$ that share an edge E. A basis function that is restricted to a single tetrahedron is in this case

$$\vec{w}_{\{E,T\}} = c_{\{E\}}\psi_{\{E,T,P_1\}}\psi_{\{E,T,P_2\}}\frac{\vec{\ell}_{\{E\}}}{V_T}, \tag{3.31}$$

where $\psi_{\{E,T,P_i\}}$ is the nodal basis function provided for point P_i, and the end points P_1 and P_2 are for the edge E as shown in Figure 3.2. Denoting $c_{\{E\}}$ as

$$c_{\{E\}} = \frac{20}{\eta\|\vec{\ell}_{\{E\}}\|} = \frac{20}{\eta\|\vec{r}_{P_2} - \vec{r}_{P_1}\|}, \tag{3.32}$$

a unit-length dipolar moment can be formulated as

$$\begin{aligned}
\vec{q}_{\vec{w}} &= \textstyle\int_\Omega \vec{w}\, dV \\
&= \textstyle\sum_{\ell=1}^{\eta} \int_{T_\ell} \vec{w}_{\{E,T_\ell\}}\, dV \\
&= c_{\{E\}} \textstyle\sum_{\ell=1}^{\eta} \frac{\vec{\ell}_{\{E\}}}{V_{T_\ell}} \int_{T_\ell} \psi_{\{E,P_1\}}\psi_{\{E,P_2\}}\, dV \\
&= c_{\{E\}} \frac{\eta\vec{\ell}_{\{E\}}}{V_{T_\ell}} \frac{V_T}{20} \\
&= \frac{\vec{\ell}_{\{E\}}}{\|\vec{\ell}_{\{E\}}\|} \\
&= \frac{\vec{r}_{P_2} - \vec{r}_{P_1}}{\|\vec{r}_{P_2} - \vec{r}_{P_1}\|}
\end{aligned} \tag{3.33}$$

It can be seen that the dipolar moment for the EW sources is actually formed similarly as for the FI sources: Defined by the opposing nodes and normalized with the distance between the nodes. The difference here is that with the EW - case the nodes share an edge whereas FI dipoles share a face. Similarly as with the linear sources, an intuitive choice for the position $\vec{r}_{\vec{w}}$ of a source dipole is in the middle of the edge, which shares points P_i and P_j.

Furthermore, it is defined that for quadratic basis functions

$$\int_{T_1} \psi_{\{E,P_i\}}\psi_{\{E,P_j\}} = \begin{cases} \frac{V_T}{10} & \text{if } i = j, \\ \frac{V_T}{20} & \text{otherwise.} \end{cases} \tag{3.34}$$

Combining the results from Equations 3.32 and 3.34, the right hand side matrix G turns to

$$\begin{aligned}
G_{\psi,\vec{w}} &= -\int_\Omega (\nabla \cdot \vec{w})\psi dV \\
&= -c_{\{E\}}\nabla\psi_{\{E,P_1\}} \cdot \frac{\vec{\ell}_{\{E,T\}}}{V_T} \sum_{\ell=1}^{\eta} \int_{T_\ell} \psi_{\{E,P_2\}}\psi_{\{E,P_j\}}\, dV \\
&\quad -c_{\{E\}}\nabla\psi_{\{E,P_2\}} \cdot \frac{\vec{\ell}_{\{E,T\}}}{V_T} \sum_{\ell=1}^{\eta} \int_{T_\ell} \psi_{\{E,P_2\}}\psi_{\{E,P_j\}}\, dV \\
&= \frac{s_{\{\psi,P_2\}} - s_{\{\psi,P_1\}}}{\|\vec{\ell}_{\{E\}}\|} = \frac{s_{\{\psi,P_2\}} - s_{\{\psi,P_1\}}}{\|\vec{r}_{P_2} - \vec{r}_{P_1}\|},
\end{aligned} \tag{3.35}$$

likewise previously presented for the FI sources. [46]

3.4 Source Configurations

In order to model a field of source currents, a given dipole position and moment can be estimated with different combinations of the synthetic source dipoles. In Figure 3.3 is presented a source configuration that consists of all the FI and EW sources from the face sharing elements of the original dipole element, resulting in 22 source dipoles and five elements in total.

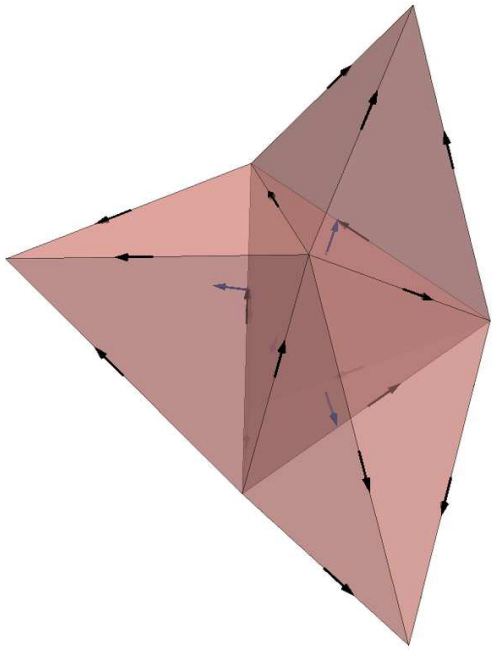

***Figure** 3.3 FI (blue) and EW (black) source dipoles in source configuration, five source elements*

3.4.1 Restricted Source Configuration

The source configuration can be adjusted in various ways. Figure 3.4 presents multiple options for the size of the patch.

One option is to take only the edges of the original dipole element, leading to six source dipoles and only one element in the configuration as presented in the upper left corner in Figure 3.4. This configuration can be expanded by adding the EW and FI dipoles from neighboring elements, resulting two to five elements and 10 - 22 dipoles in the source set-up. In addition, this can be further expanded with the neighbor elements of the neighbors.

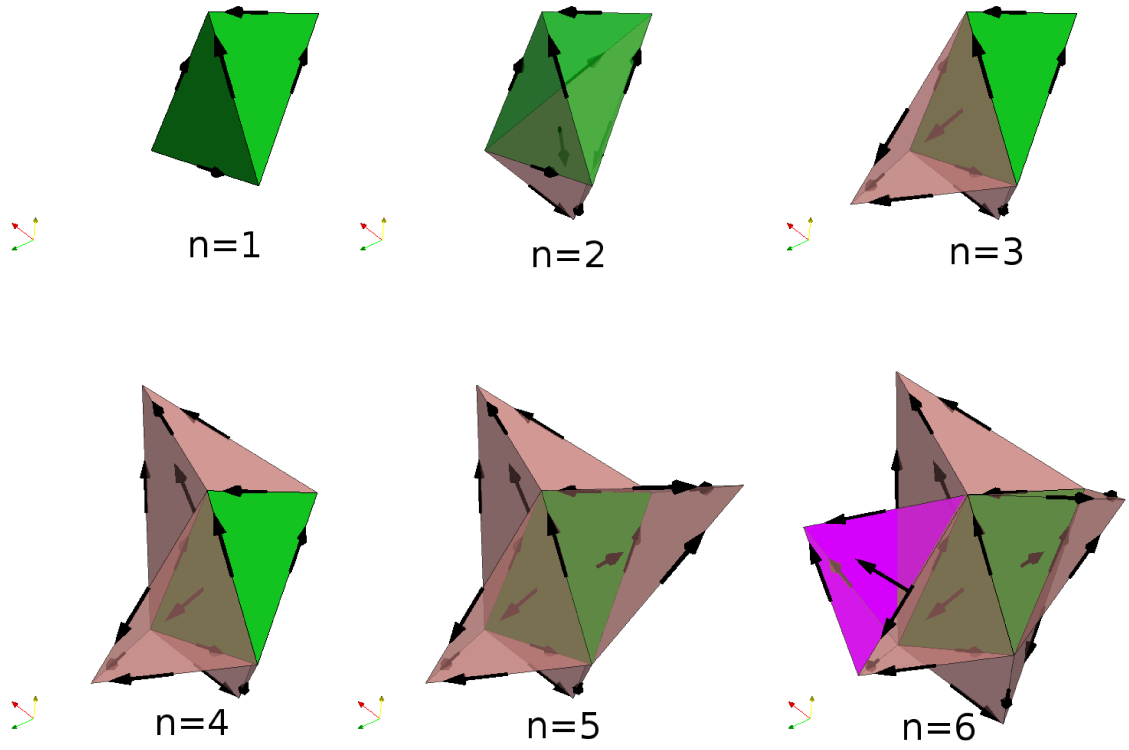

Figure 3.4 *Source configurations with $n = 1, \ldots, 6$ elements with FI and EW dipoles. The element for the original given dipole is marked with green, and the purple element is added with adaptive style.*

One of these cases is presented in lower right corner in Figure 3.4. This scenario is described later on in Subsection 3.4.2. In this study, one goal is to investigate how the number of the source elements affects the forward model accuracy.

On the other hand, the source configuration presented in Figure 3.3 might be problematic when the given dipole is too close to the brain compartment boundary. In this scenario, some of the synthetic dipoles are located in the next compartment as illustrated in the upper part of Figure 3.5. This might result in major errors in the forward model output if the conductivity values of the layers differ notably. This situation could be avoided by considering a limited version in which those source dipoles in the wrong compartment are rejected and approximating the given dipole with a smaller amount of source dipoles, and this design is displayed in the lower part of Figure 3.5. The restriction might lead to changed results if, for example, the gray matter layer in the mesh is very thin (as in reality in the human brain) and therefore the resulting source patch contains too few source dipoles. Although the resulting source model can be truly focal, the orientation and magnitude estimates might alter. This motivates to investigate different approaches for source configurations, and one of them is presented in the next section.

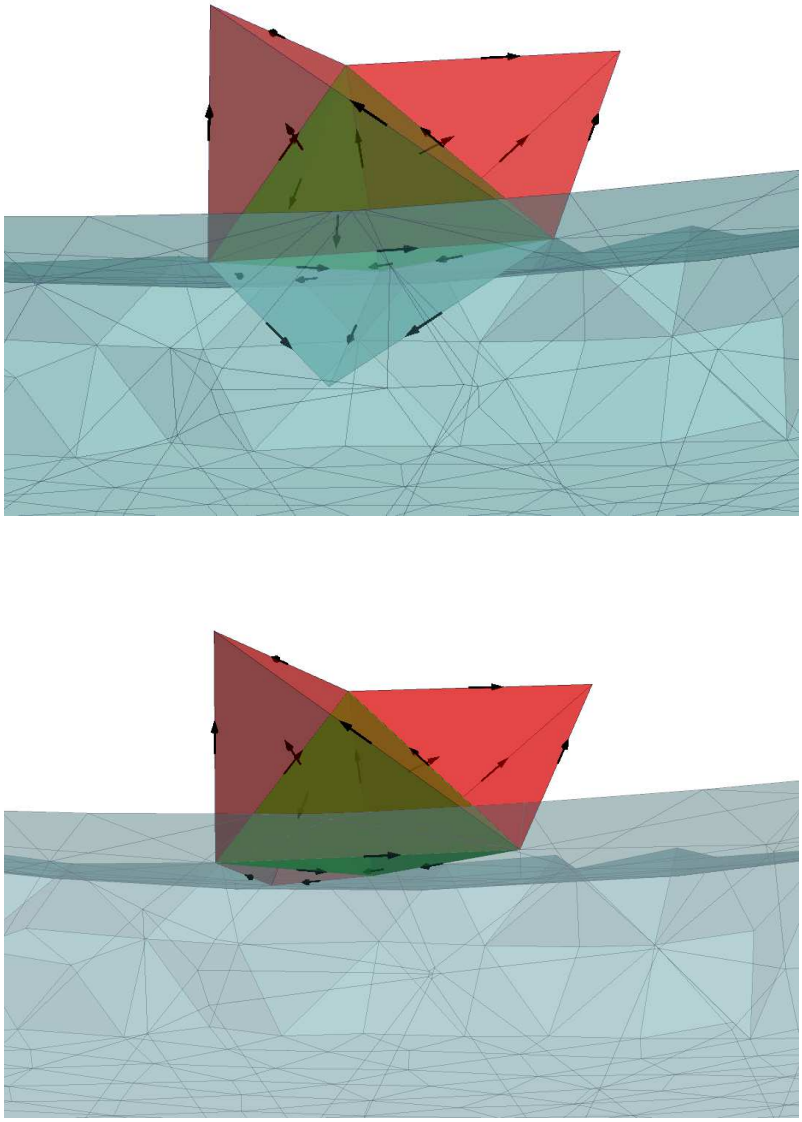

Figure 3.5 *The source configuration with FI and EW dipoles near the gray matter boundary. The upper figure presents the case where the sources are not limited in the gray matter area. Correspondingly, in the lower figure the restriction is set.*

3.4.2 Adaptive Source Configuration

In this thesis, the H(div) -approach model is developed further with an adaptive version of the configuration. This approach has a similar structure as the earlier presented version. Like previously, the aim to have a mixture of the face intersecting and edgewise dipoles surrounding the given dipole position. Unlike with the previously presented restricted version, the source elements in this case are chosen with an adaptive style.

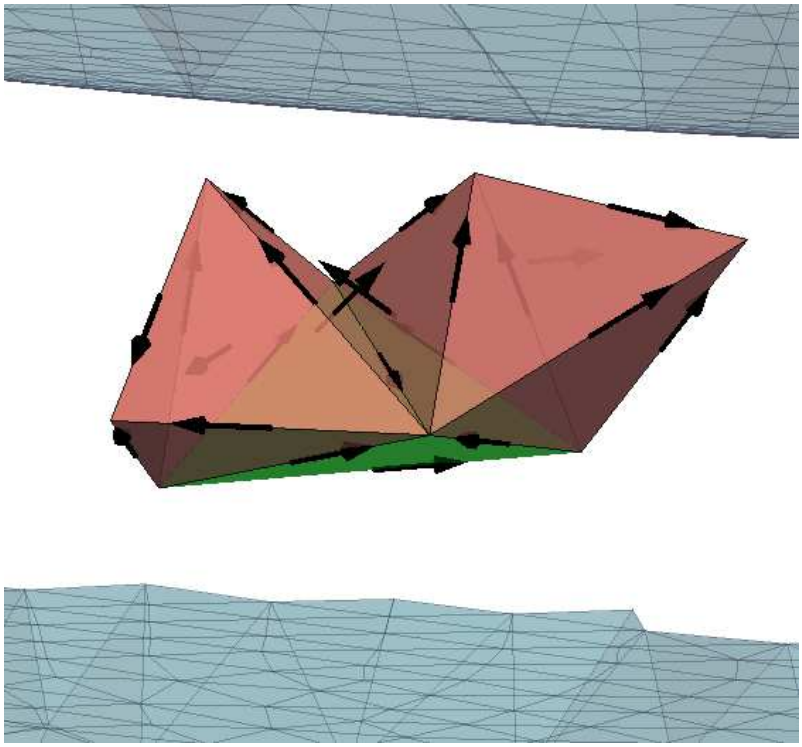

Figure 3.6 *An example of an adaptive source configuration*

The adaptive version is created as follows: If the neighbor that shares a face with the original dipole element has neighbors that are over layer boundary (e.g. over gray matter), this neighbor of the original element is rejected from the source configuration. This applies also if some node of the face-sharing neighbor is too close to the boundary. Instead, the configuration is extended with the FI and EW sources from neighbor's neighbors that are within suitable distance of the boundary. These neighbor's neighbors are also chosen based on the distance to the original given dipole, and the closest element is chosen in the configuration. An example of an adaptive configuration is presented in Figure 3.6. Moreover, the proximity criteria for element nodes being too close to the boundary is set with a tolerance parameter that can be adapted depending on the length of the element edges. Likewise with restricted modeling type, the amount of the source elements can be varied as desired. A scenario with an additional sixth element is presented in lower right corner in Figure 3.4.

3.5 Interpolation with Source Dipoles

In order to simulate an arbitrary dipolar source with a position $\vec{r}$ and a moment $\vec{p}$ by divergence conforming source models, it is needed to apply an interpolation technique for creating an estimate. This is done by taking a superposition of the

source dipole positions and moments as $\vec{p} \approx \sum_{\ell=1}^{S} c_\ell \vec{q}_{\vec{w}_\ell}$ and $\vec{r} \approx \sum_{\ell=1}^{S} c_\ell \vec{r}_{\vec{w}_\ell}$, in which S is the amount of source dipoles and c_ℓ are interpolation coefficients. As a result, the outcome is a linear combination of divergence conforming sources that represents the given source dipole orientation and position. [46] The interpolation technique applied here is called Position Based Optimization (PBO).

The aim of the PBO is to find the coefficient vector $\mathbf{c} = (c_1, c_2, \ldots, c_S)$ that solves

$$\min_{\mathbf{c}} \sum_{\ell=1}^{S} {c_\ell}^2 \omega_\ell^2, \tag{3.36}$$

with a condition that

$$\mathbf{Q} = \mathbf{cp}. \tag{3.37}$$

Here the parameters ω_ℓ are weighting coefficients, defined by $\omega_\ell = \|\vec{r}_{\vec{w}_\ell} - \vec{r}\|$ and the matrix $\mathbf{Q}$ is formed by dipolar moments $\mathbf{Q} = \mathbf{q}_{\vec{w}_1}, \mathbf{q}_{\vec{w}_2}, \ldots, \mathbf{q}_{\vec{w}_S}$. The condition from Equation 3.37 makes sure that the interpolated and actual dipoles have coinciding orientations. The minimizing problem 3.36 can be solved with applying the Lagrangian multipliers method, resulting in the linear system

$$\begin{pmatrix} \mathbf{D} & \mathbf{Q^T} \\ \mathbf{Q} & \mathbf{0} \end{pmatrix} \begin{pmatrix} \mathbf{c} \\ \mathbf{d} \end{pmatrix} = \begin{pmatrix} \mathbf{0} \\ \mathbf{p} \end{pmatrix}, \tag{3.38}$$

where the matrix $\mathbf{D}$ is a diagonal $\mathbf{D} = \mathrm{diag}(\omega_1^2, \omega_2^2, \ldots, \omega_S^2)$, and $\mathbf{d}$ is an auxiliary vector. [46] The coefficient vector $\mathbf{c}$ can be solved from linear system 3.38 with e.g. the method of QR decomposition.

3.6 Classical Methods for Approximating Source Currents

In addition to H(div) source approach, the EEG sources can be estimated with monopolar-based approximations. In this section, the partial integration (PI) and St. Venant (SV) dipole estimation methods are presented.

3.6.1 Partial Integration

The partial integration is a feasible method for source modeling if the aim is to find highly focal dipole estimates. With partial integration, the primary current source is approximated with monopolar sources, resulting in four nodes in the source configuration. As the goal is to find the load vector $\mathbf{f}$ of Equation 3.12, the right

hand side of Equation 3.6 can be partially integrated as

$$f_i = \int_\Omega (\nabla \cdot \vec{J}^P)\psi_i \, dV = \int_\Omega \vec{J}^P \cdot \nabla\psi_i \, dV - \int_{\partial\Omega} \partial_{\mathbf{n}} \vec{J}^P \cdot \psi_i \, dS. \tag{3.39}$$

As the current $\vec{J}^P$ is zero on the surface of the volume conductor, the last term in the Equation 3.39 vanishes, resulting in

$$f_i = \int_\Omega \vec{J}^P \cdot \nabla\psi_i \, dV = \begin{cases} \vec{p} \cdot \nabla\psi_{i|\vec{r}}, & \text{if } \vec{r} \text{ in support of } \psi_i, \\ 0, & \text{otherwise.} \end{cases} \tag{3.40}$$

[46]

3.6.2 St. Venant Method

The basic idea of the St. Venant method is to approximate a dipole moment $\vec{p}$ at a point $\vec{r}$ based on monopolar loads $m_0, m_1, \ldots, m_M$ on M neighboring FE nodes, resulting in the dipolar moment being fulfilled and also, regular source load.[37] As these loads are located at the finite element mesh nodes $\vec{r_0}, \vec{r_1}, \ldots, \vec{r_M}$, where $\vec{r_0}$ is the closest node to $\vec{r}$ and the rest $\vec{r_1}, \vec{r_2}, \ldots, \vec{r_M}$ share an edge with $\vec{r_0}$. Remembering that the law of the total charge conservation results in $\nabla \cdot \vec{J} = 0$, for monopolar effect it yields that

$$\sum_{i=0}^{M} m_i = 0. \tag{3.41}$$

Furthermore, for the dipole moment $\vec{p}$ the condition is

$$\frac{1}{\alpha}\vec{p} = \sum_{i=0}^{M} \frac{m_i}{\alpha}(\vec{r_i} - \vec{r}), \tag{3.42}$$

where α is a reference distance, being at least double the length of the longest edge in the FE mesh. And finally, taking into account the suppression of higher order moments

$$\sum_{i=0}^{M} \frac{m_i}{\alpha^2}[(\vec{r_i} - \vec{r}) \cdot \vec{e_j}]^2 = 0 \quad \text{for} \quad j = 1, 2, 3. \tag{3.43}$$

[46]

A commonly used method to find the load vector $\mathbf{m} = (m_1, m_2, \ldots, m_M)$ is by forming the regularized least-squares estimate $\mathbf{m} = (\mathbf{P}^T\mathbf{P} + \lambda\mathbf{D})^{-1}\mathbf{P}^T\mathbf{b}$, in which the vector $\mathbf{b}$ is

$$\mathbf{b} = \begin{pmatrix} \mathbf{b}_1 \\ \mathbf{b}_2 \\ \mathbf{b}_3 \end{pmatrix} \quad \text{and} \quad \mathbf{b}_j = \begin{pmatrix} 0 \\ \alpha^{-1} p_j \\ 0 \end{pmatrix}, \tag{3.44}$$

and similarly,

$$\mathbf{P} = \begin{pmatrix} \mathbf{P}_1 \\ \mathbf{P}_2 \\ \mathbf{P}_3 \end{pmatrix} \quad \text{with} \quad \mathbf{P}_j = \begin{pmatrix} 1 & \cdots & 1 \\ \alpha^{-1}(\vec{r}_1 - \vec{r}) \cdot \vec{e}_j & \cdots & \alpha^{-1}(\vec{r}_M - \vec{r}) \cdot \vec{e}_j \\ \alpha^{-2}[(\vec{r}_1 - \vec{r}) \cdot \vec{e}_j]^2 & \cdots & \alpha^{-2}[(\vec{r}_M - \vec{r}) \cdot \vec{e}_j]^2 \end{pmatrix}. \tag{3.45}$$

The regularization matrix $\mathbf{D}$ is defined as $\mathbf{D} = \mathrm{diag}(\|\vec{r}_1 - \vec{r}\|^2, \|\vec{r}_2 - \vec{r}\|^2, \ldots, \|\vec{r}_M - \vec{r}\|^2)$, and adjusted with the regularization parameter $\lambda > 0$. The amount of conditions for St. Venant is 7. [46] In this thesis, the St. Venant method is applied in a way that the nodes over gray matter compartment are rejected.

3.7 Performance Measures

For the multi-layer spherical model, there exist analytical models for the potential caused by a mathematical point dipole. After having the analytical solution computed, the results of the forward FEM computations can be analyzed by using the relative difference and magnitude measures (RDM and lnMAG). Finally, the error series for different source models are further analyzed with the statistical Mann-Whitney U-test in order to show the statistically significant differences between models.

3.7.1 Analytical Solution

In this study, the analytical model utilized was originally derived by De Munck and Peters [41], and the solution is harnessed for assessing the accuracy of different source models. Here the analytical model is presented with a brief overlook, an extended description can be found from Reference [41].

Instead of tetrahedral mesh, the analytical model is constructed with N nested shells, and the radius for these shells are $r_1 < r_2 < \cdots < r_N$. The conductivity values for both radial and tangential directions are constant, i.e. $\sigma^{rad}(\mathbf{x}) = \sigma_j^{rad} \in \mathbb{R}^+$ and $\sigma^{tan}(\mathbf{x}) = \sigma_j^{tan} \in \mathbb{R}^+$ for each of the shells. Here the radial component $x^r \in \mathbb{R}$ of

the vector $\mathbf{x}$ is defined as $r_j < x^r < r_{j+1}$, expressly that x^r is the distance to the origin of the sphere. In addition, it is presumed that the source is located closer to the origin of the sphere than the electrodes for measurements. The positions of electrodes are denoted by $\mathbf{v}_i$ with $i = 1, \ldots, L$ where L is the amount of electrodes. The radial coordinate of an electrode is $y_i^r \in \mathbb{R}$. Subsequently, a source dipole at position $\mathbf{x}$ and with moment $\vec{p}$ invokes a potential at $\mathbf{v}_i$ that is approximated as

$$y(\mathbf{x}, \vec{p}, \mathbf{v}_i) = \frac{1}{4\pi}\langle \vec{p}, \frac{S_0}{v_i^r}\mathbf{v}_i + (\frac{S_1}{x^r} - \cos\omega_{x,v_i}\frac{S_0}{x^r})\mathbf{x}\rangle, \tag{3.46}$$

in which ω_{x,v_i} is the angular distance between $\mathbf{x}$ and $\mathbf{v}_i$. If the center of a sphere is in the origin, the distance ω_{x,v_i} can be written as $\omega_{x,v_i} = \arccos(\langle \frac{\mathbf{x}}{\|\mathbf{x}\|_2}, \frac{\mathbf{v}_i}{\|\mathbf{v}_i\|_2}\rangle)$. Furthermore, the terms S_0 and S_1 are defined as

$$S_0 = \frac{F_0}{x^r}\frac{\Lambda}{(1 - 2\Lambda\cos\omega_{x,v_i} + \Lambda^2)^{\frac{3}{2}}} + \frac{1}{x^r}\sum_{n=1}^{\infty}[(2n+1)R_n(x^r, v_i^r) - F_0\Lambda^n]P_n'(\cos\omega_{x,v_i}), \tag{3.47}$$

and

$$S_1 = F_1\frac{\Lambda cos\omega_{x,v_i} - \Lambda^2}{(1 - 2\Lambda\cos\omega_{x,v_i} + \Lambda^2)^{\frac{3}{2}}} + \sum_{n=1}^{\infty}[(2n+1)R_n'(x^r, v_i^r) - F_1 n\Lambda^n]P_n(\cos\omega_{x,v_i}), \tag{3.48}$$

where P_n is the Legendre polynomial and P_n is the corresponding derivative. Moreover, the coefficient terms R_n and their derivatives R_n' can be calculated analytically. The exact forms for terms F_0, F_1, and Λ are presented in Reference [41] in a detailed manner. Also, there is set a break criteria for computing the infinite series of Equations 3.47 and 3.48. Finally, the outcome is a vector of electrode potentials, denoted as $\mathbf{y}_{\text{ana},i} = y(\mathbf{x}, \vec{p}, \mathbf{v}_i)$ with $i = 1, \ldots, L$.[50]

3.7.2 The Relative Difference Measure Percent (RDM%)

The relative difference measure RDM indicates how the analytical and numerical dipole approximations differ in positional and directional aspects. When it comes to source detection, RDM reveals the error for location and orientation. The RDM in percent can be formulated as

$$\text{RDM\%}(\mathbf{y}_{\text{ana}}, \mathbf{y}_{\text{FEM}}) = \frac{100}{2}\left\| \frac{\mathbf{y}_{\text{ana}}}{\|\mathbf{y}_{\text{ana}}\|_2} - \frac{\mathbf{y}_{\text{FEM}}}{\|\mathbf{y}_{\text{FEM}}\|_2} \right\|_2. \tag{3.49}$$

The multiplication factor $\frac{100}{2}$ transforms the RDM model to RDM%, since RDM is bounded between 0 (there is no error) and 2 (here $\mathbf{y}_{\text{ana}} = \mathbf{y}_{\text{FEM}}$). [46]

3.7.3 The Logarithmic Magnitude Error Percent (lnMAG%)

The logarithmic magnitude error (lnMAG) estimates the difference in magnitude between the modeled and analytical solution. The lnMAG error percent is

$$\mathrm{lnMAG\%}(\mathbf{y}_{\mathrm{ana}}, \mathbf{y}_{\mathrm{FEM}}) = 100 \ln \left(\frac{\left\|\mathbf{y}_{\mathrm{FEM}}\right\|_2}{\|\mathbf{y}_{\mathrm{ana}}\|_2}\right). \tag{3.50}$$

As the relation $\ln(1+x) \approx x$ holds for small $|x|$, the Equation 3.51 can be written as

$$\mathrm{lnMAG\%}(\mathbf{y}_{\mathrm{ana}}, \mathbf{y}_{\mathrm{FEM}}) = 100\left(\frac{\left\|\mathbf{y}_{\mathrm{FEM}}\right\|_2}{\|\mathbf{y}_{\mathrm{ana}}\|_2}\right) - 100. \tag{3.51}$$

[46]

3.7.4 Mann-Whitney U-test

After computing the RDM and lnMAG percents, the statistically significant mutual differences between source models are also evaluated with the Mann-Whitney U-test. [38] The non-parametric Mann-Whitney U-test reveals whether there exist differences that are more or less meaningful, in place of random differences.

The Mann - Whitney U - test evaluates two data sets with a certain confidence level $1-\alpha$, e.g. $\alpha \approx 0.05$. At first it is assumed that two samples X and Y are independent, and that the size of the sample X is n_X. Correspondingly, n_Y denotes the size of the sample Y. Variable U is the amount of times when $y \in Y$ bypasses an $x \in X$ in an ordered line of the elements in the two samples X and Y. This can be written as

$$U = W - \frac{n_X(n_X+1)}{2}. \tag{3.52}$$

Based on Equation 3.52, the z-statistics can be computed as

$$z = \frac{W - E(W)}{\sqrt{V(W)}} = \frac{W - [\frac{n_X(n_Y+n_X+1)}{2}] - 0.5 * \mathrm{sign}(W - \frac{n_X(n_Y+n_X+1)}{2})}{\sqrt{\frac{n_X n_Y[(n_X+n_Y+1)-TS]}{12}}}, \tag{3.53}$$

in which $\mathrm{sign}(i)$ stands for the signum function that returns the sign of the variable i ($+, -$ or 0). Also, TS is a tie adjustment parameter, defined as

$$TS = \frac{\sum_{j=1}^{g}(t_j-1)t_j(t_j+1)}{(n_X+n_Y)(n_X+n_Y-1)}. \tag{3.54}$$

Here g is the amount of tied groups and t_j denotes the size of tied group j. Finally the p-value is computed with the help of the standard normal distribution. If the

p-value is lower than α, there is a significant mutual difference between two sample sets. Correspondingly, $p \geq \alpha$ suggests that the differences are not statistically remarkable. [34, 39]

3.7.5 Boxplot

The outcomes of the different source models are evaluated by comparing them to the analytical solution. The RDM and lnMAG percents are drawn with boxplot - diagrams (or known also as box-and-whisker plot). With boxplot, the median is marked as a center line in the box, and the box boundaries are set to lower 25% and upper 75 % quantiles. The total range i.e. minimum and maximum values of the data set is drawn with vertical lines, known as whiskers. In this thesis, the total range is limited by rejecting outliers with a 1.5IQR rule. The 1.5IQR rule is defined with an interquartile range (IQR), that is the difference between the third and first quantile, in this case the difference between $Q_1 = 25\%$ and $Q_3 = 75\%$. The whisker limits are then denoted as the highest and lowest value of the data set that fit in between the lower bound $Q_1 - 1.5 * IQR$ and upper bound $Q_3 + 1.5 * IQR$. However, the rejected outliers are shown with separate markers. [36]

4. IMPLEMENTATION

The forward EEG model scenarios were simulated with a C++ toolbox DUNE (the Distributed and Unified Numerics Environment). [17, 15, 10, 9]. The scripts for partial integration and St. Venant already existed for DUNE, and therefore only the restricted and adaptive divergence conforming source models were implemented.

4.1 DUNE

As an open source software for solving partial differential equations, DUNE provides a basis for easy implementations for e.g. finite element method, finite volume method, and finite difference method. The elementary concept of DUNE is to construct easy interfaces that allow using and combining efficiently both the current, and new DUNE libraries. As the modern C++ programming techniques are harnessed in DUNE, it is possible to design several varying implementations of the same concept, i.e. different setup's for grids or solvers. This all can be created with a common interface via a low overhead.[4]

4.2 duneuro

duneuro is a DUNE based toolbox for solving MEG and EEG forward problems. [1, 26, 45] It has been developed in Münster in collaboration between the Faculty of Mathematics and Computer Science at the University of Münster, and the Institute for Biomagnetism and Biosignalanalysis of the Medical Faculty at the University of Münster. At the time this thesis is written, duneuro is not yet in open distribution, but available when asked. duneuro is also constructed with C++, and controlled here via an interface with MATLAB software [40].

4.2.1 duneuro Implementation

One objective of this thesis project was to create a duneuro script for FI and EW sources. As the presented formulations of FI and EW sources apply only on tetrahedral mesh, the script was restricted to operate only on tetrahedral meshes. Like

other duneuro blocks, the script is not currently available in open distribution, but can be delivered for requests.

In this study, the mesh is chosen to be a tetrahedral conforming mesh, presented with DUNE-ALUGrid module [6]. Moreover, the partial differential equation is discretized with DUNE-PDELab module [11]. In addition, the solver type is set to the fitted continuous Galerkin, which refers to the formulation of the finite element system. An extensive description of the continuous Galerkin approach can be found e.g. in Reference [50]. As the linear system 3.11 is relatively large, it is more appropriate to solve the system with a conjugate gradient method (CGM) equipped with an algebraic multigrid preconditioner (AMG).[54, 37] Here the preconditioner applied is the symmetric successive overrelaxation (SSOR) that operates as a smoother. [16] The CGM iteration rounds are stopped when the stopping criteria is fulfilled, and the limit is defined with residual $\|\mathbf{Gx} - \mathbf{Az}\|_2$. In this thesis, the stopping criteria was set to 10^{-8}.

The general structure of the EEG forward problem implementation in duneuro is presented in Figure 4.1.

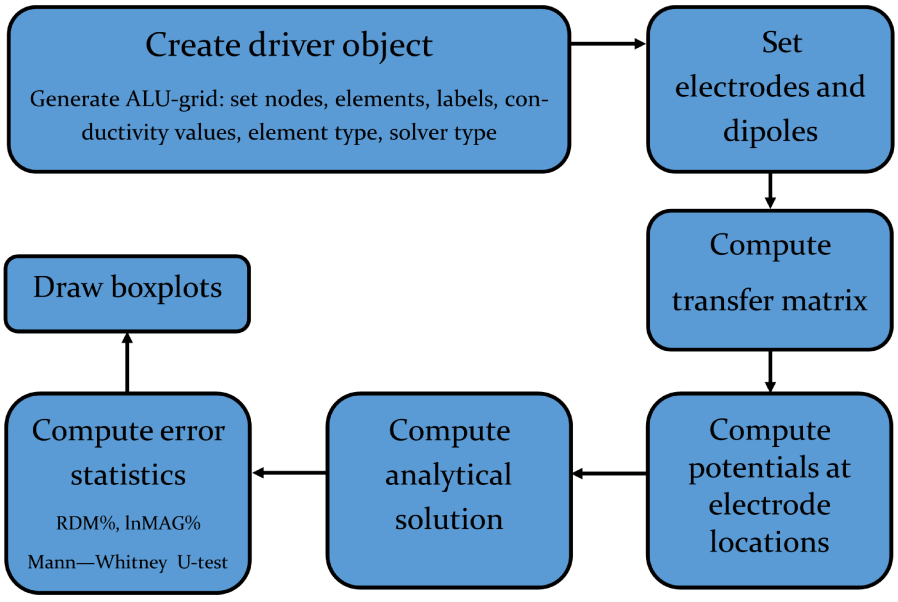

Figure 4.1 *The process of the duneuro implementation for the EEG forward problem*

The algorithm presented in Figure 4.1 describes the implementation in a simplified

manner for a single source model method. A more detailed description is shown in an example script of duneuro implementation for the MATLAB interface, which is presented later on in Appendix A.

4.3 Grids and Parameters

In the interest of testing the methods, there were two separate dipole data sets created with varying eccentricity values. Eccentricity refers to the relative distance from the center of the brain in respect of the gray matter layer boundary. The first dipole set included 500 dipole moments and locations for eccentricities 20, 40, 60, 80 and 99.9 %, i.e. 100 for each. Having the dipoles located in all those locations in the sphere gives information on how the source models perform for brain activity in all locations. The second set consisted only of dipoles with eccentricity 99.9 % (i.e., 0.78 millimeters away from the outer gray matter surface), and the amount of dipoles was set to 200. Here the idea is to compare the model performance with sources located extremely close to the gray matter boundary.

The spherical mesh applied in this study is designed for testing the new adaptive approach with a special thin cortex layer. The model is presented in Figure 4.2.

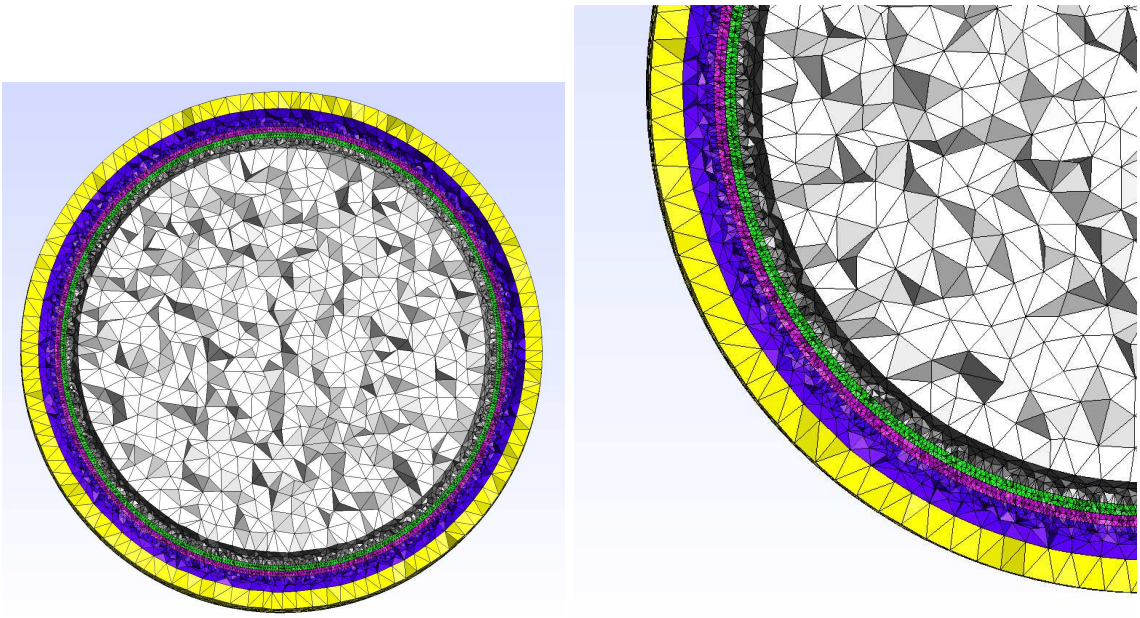

Figure 4.2 *A visualization of the spherical grid used for modeling*

As shown in Figure 4.2, there are altogether six layers: white matter (marked with white elements), inner gray matter (dark gray), thin cortex (green), CSF (purple),

skull (blue), and scalp (yellow). This model is discretized with FE mesh consisting of 5555777 elements and 907788 nodes. In addition, there were 120 points taken on the sphere surface as electrode locations.

The radii and conductivity values for all layers are presented in Table 4.1.

Compartment	Outer shell radius (mm)	Conductivity (S/m)
Scalp	92	0.33
Skull	86	0.0042
CSF	80	1.79
Cortex	78	0.33
Inner gray matter	76	0.33
White matter	72	0.33

Table 4.1 *The sphere radii and conductivity values for mesh compartments*

Although it would be more coherent to model the white matter layer as an anisotropic one, that aspect is omitted here. This is due to the fact that at the time the numerical analysis was accomplished, there existed no possibility to model anisotropy with duneuro MATLAB interface.

Both restricted divergence conforming and St. Venant source models were implemented with a restriction to the brain compartment where the given dipole is located, meaning that the nodes and elements over the layer boundary were rejected. As mentioned in Chapter 3, the impact of the amount of the source elements is evaluated in this study. In the first place, the divergence conforming source dipoles are tested with a varying amount of elements. Starting from only one element (original dipole element), the amount is increased all the way to the full five elements in source set-up, meaning that all face sharing neighbors of the original dipole element are included. However, the restriction for rejecting the elements outside the layer is applied, causing that some of the intended full configurations remain short. In addition, the adaptive version is tested via a similar approach with varying patch size, also with the six-element case. In addition, the adaptive version is compared to the regular, restricted version with all five elements included in configuration.

Furthermore, the Mann-Whitney U-test is applied to the RDM% and lnMAG% series with $\alpha = 0.05$, representing 95 % confidence level. The tests are carried out with MATLAB [40] *ranksum* - function. [39]

5. RESULTS

The results for the numerical experiments are presented in this chapter. The boxplots for RDM% and lnMAG% are analyzed for both restricted and adaptive divergence conforming source models with the varying number of source elements. These results are also compared to the results obtained with other source models, St. Venant and partial integration. After this, the statistically significant differences between source model errors are evaluated via Mann-Whitney U-tests and the results are shown in tables.

5.1 The Results of the Restricted Source Model

The RDM and the lnMAG percents for the restricted models with $n = 1, \ldots, 5$ patch elements in source configuration with the first dipole set with 100 dipoles for each eccentricity 20, 40, 60, 80, and 99.9 %, are presented in Figures 5.1 and 5.2.

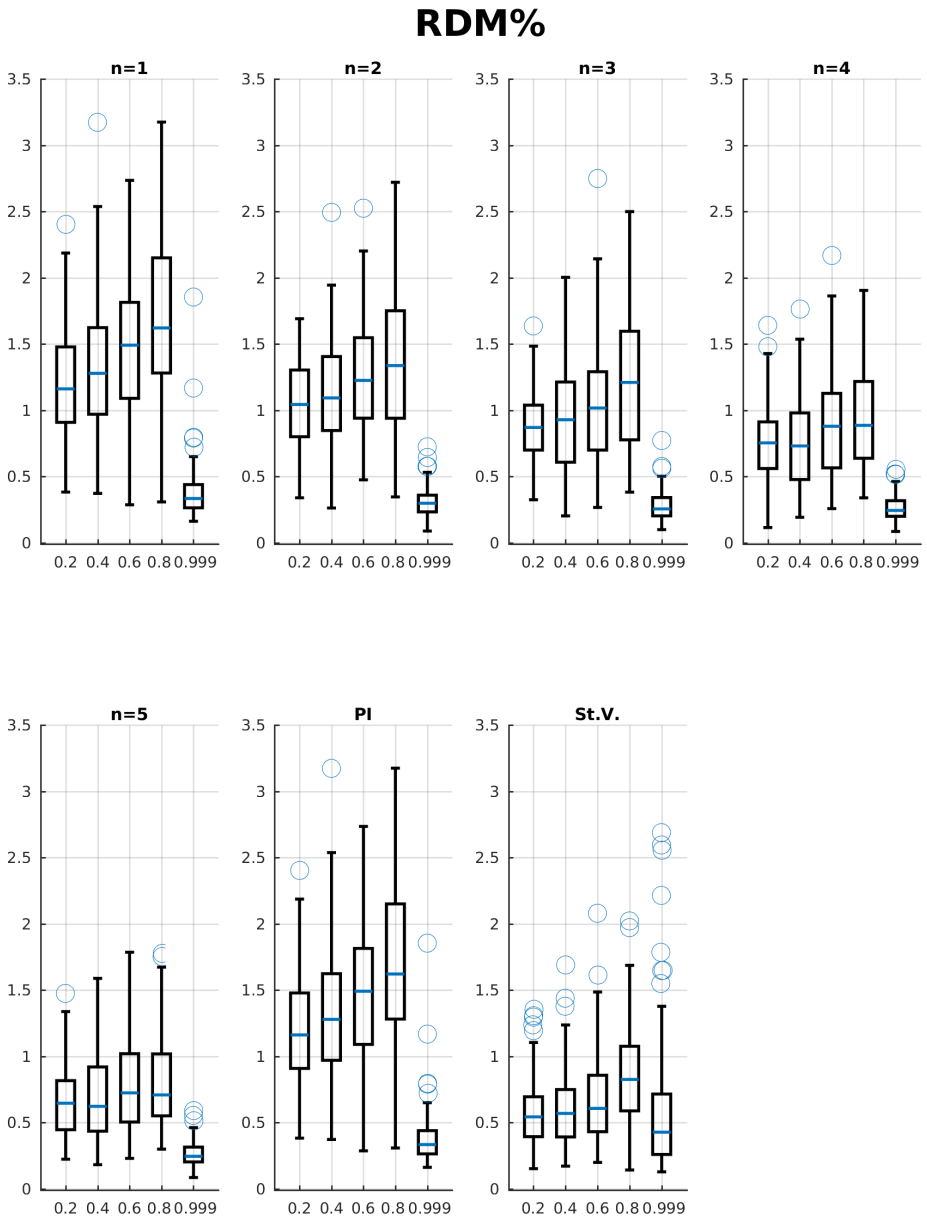

Figure 5.1 *The RDM% for the restricted source model with n elements in source configuration with dipoles at eccentricities 20, 40, 60, 80, and 99.9 %. Also, the results with partial integration and St. Venant are included.*

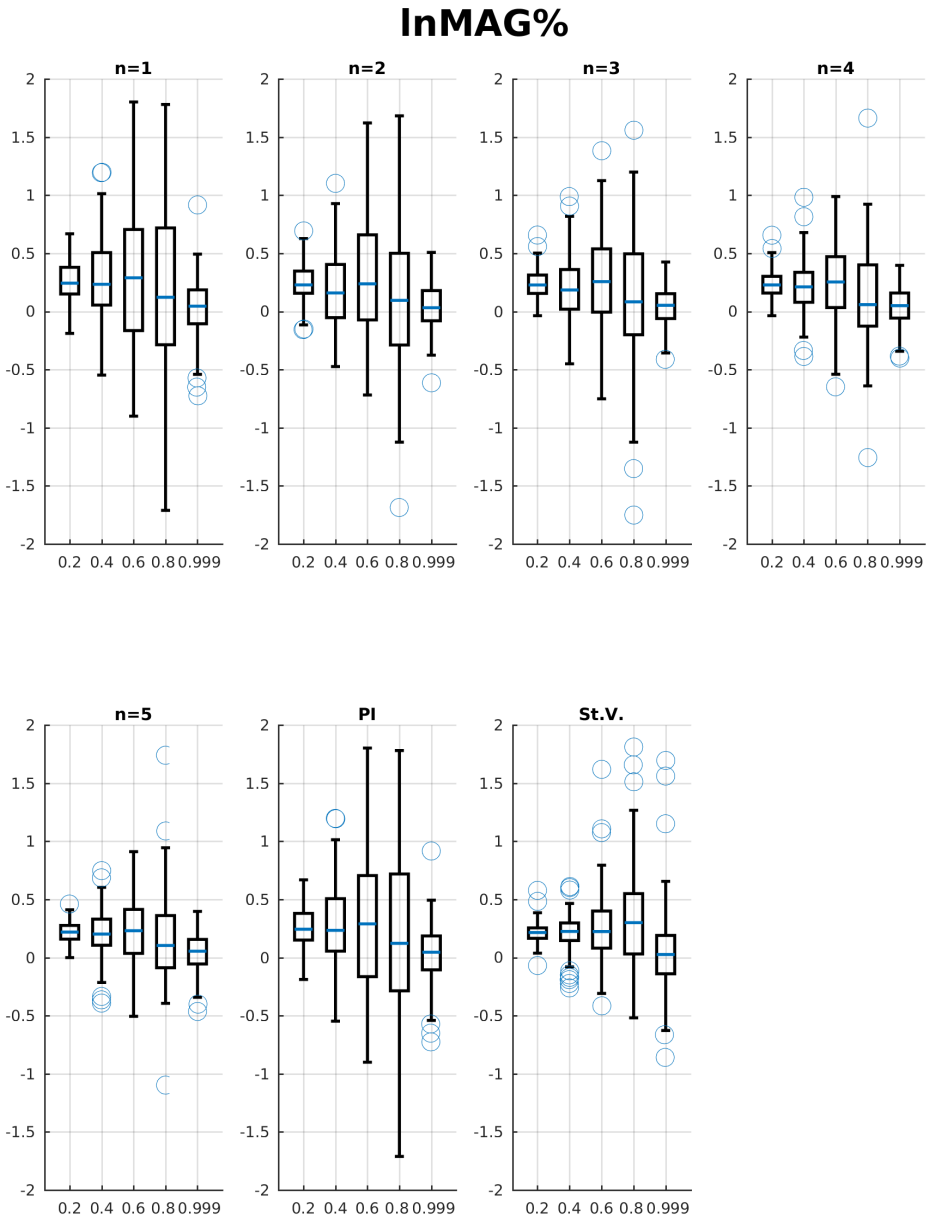

Figure 5.2 *The lnMAG% for the restricted source model with n elements in source configuration with dipoles at eccentricities 20, 40, 60, 80, and 99.9 %. Again, the results with partial integration and St. Venant are included.*

Along with the Figures 5.1 and 5.2, the median values of the RDM% and lnMAG% for all eccentricities are presented in Table 5.1.

RDM%							
eccentricity	n = 1	n = 2	n = 3	n = 4	n = 5	PI	St.V.
20 %	1.16	1.04	0.87	0.75	0.65	1.16	0.54
40 %	1.28	1.09	0.93	0.73	0.62	1.28	0.57
60 %	1.49	1.22	1.02	0.88	0.72	1.49	0.61
80 %	1.62	1.34	1.21	0.89	0.71	1.62	0.82
99.9 %	0.33	0.30	0.25	0.24	0.24	0.33	0.43
lnMAG%							
eccentricity	n = 1	n = 2	n = 3	n = 4	n = 5	PI	St.V.
20 %	0.24	0.23	0.23	0.23	0.22	0.24	0.22
40 %	0.23	0.16	0.18	0.21	0.20	0.23	0.22
60 %	0.29	0.24	0.26	0.25	0.23	0.29	0.22
80 %	0.12	0.10	0.08	0.06	0.10	0.12	0.30
99.9 %	0.04	0.03	0.05	0.05	0.05	0.05	0.03

Table 5.1 *The median values of the RDM% and lnMAG% for the restricted source models with n elements with 100 test dipoles at each eccentricity*

When modeling the electrode potentials that are generated by dipoles at low eccentricities (0 - 60 %), the St. Venant source model seems to produce the most accurate results. The total ranges of the RDM % errors shown in Figure 5.1 at eccentricities 0 - 60 % are the most narrow with the St. Venant model. Moreover, for eccentricities 0 - 60 % St. Venant has the lowest RDM % median values, 0.54 - 0.61 % as can be seen in Table 5.1. The same trend can be observed for the lnMAG % error in Figure 5.2 and Table 5.1. However, the difference to the five-element version of the restricted dipolar source model is not highly remarkable. The poorest precision is obtained with partial integration and the restricted source model with one element in source configuration.

On the other hand, at eccentricity 80 % the restricted H(div) - source model with five patch elements outperforms the St. Venant model, both in respect of RDM% and lnMAG%. In the same way, the accuracy at eccentricity 99.9 % is far better with the H(div) source models than with St. Venant. Actually, in this study St. Venant seems to produce the least accurate results based on the RDM% errors when the dipoles are located near the outer gray matter boundary.

Generally, the outcome of the restricted divergence conforming source model seems to improve as the amount of dipole elements is increased. Although there are no great

differences seen in terms of magnitude errors, the errors for location and direction (i.e. RDM %) indicate that bigger element patches result in more precise potential values than smaller patches. In addition, it is noteworthy how the results of partial integration and the divergence conforming dipolar source model with one patch element are identical.

Likewise, the RDM and the lnMAG percents for the same set up but with 200 dipoles at eccentricity 99.9 % are presented in Figure 5.3.

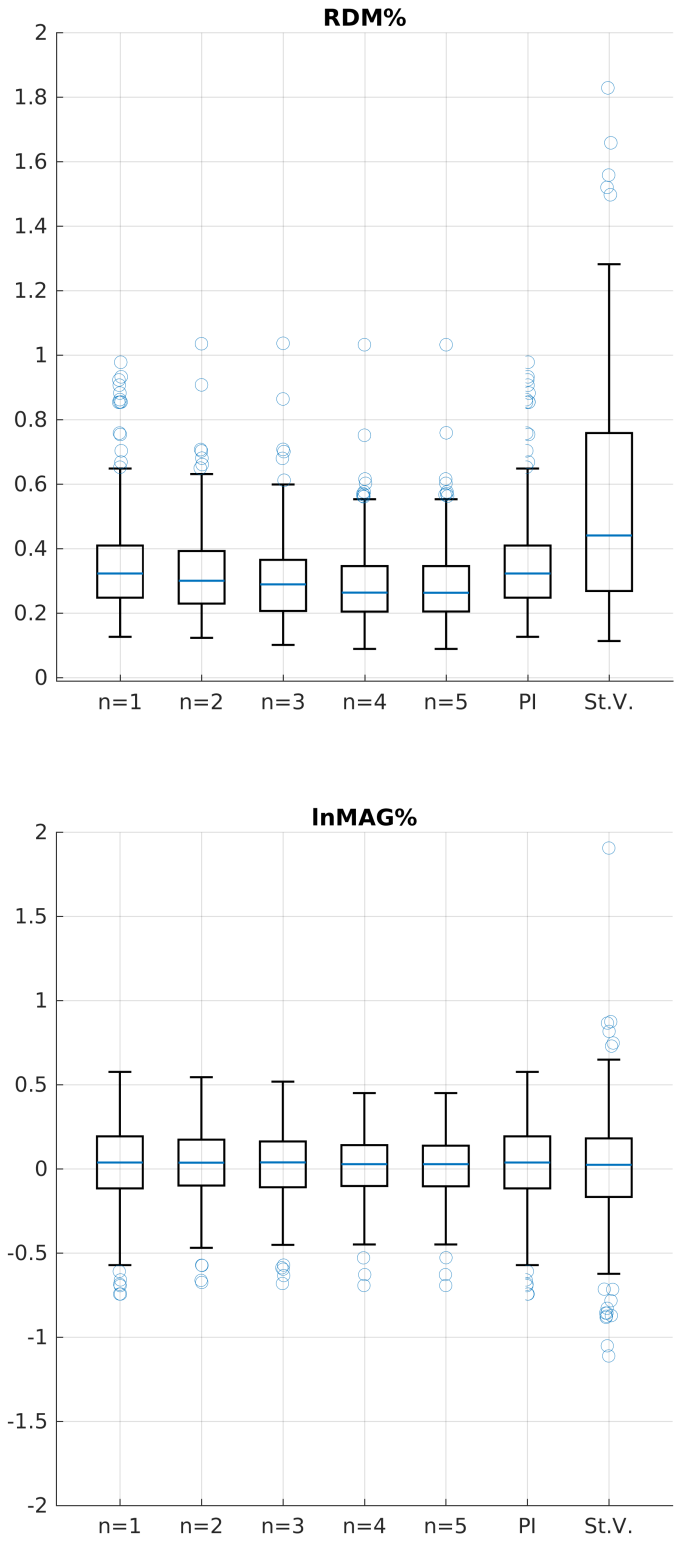

Figure 5.3 *The RDM% (upper figure) and the lnMAG% (lower figure) for the restricted source model with n elements in source configuration, for partial integration and for St. Venant with 200 dipoles at eccentricity 99.9 %.*

As seen in Figure 5.3, the lowest position error, i.e. RDM% is obtained with the source model with five source elements. However, the difference to the four-element model is infinitesimal. Moreover, the highest position error is achieved with the St. Venant model. With the St. Venant, the amount of outliers in boxplot is also highest, meaning that there could be a risk of biased results with St. Venant model if the dipole is extremely close to the layer boundary. As noticed previously, the RDM percents for partial integration and one-element source model are uniform. Further investigation revealed that the potentials generated with these models are almost the same: the maximum difference between the electrode potentials of partial integration and the dipolar source model with one element was approximately $5 \cdot 10^{-12}$ volts.

In turn, the lnMAG% medians for all source models are relatively close to each other. The lowest lnMAG % error median, 0.024 % is achieved with St. Venant, but the total range is wider than with other source models. The following lowest error is with source models with four and five elements, 0.027 %.

The results of the Mann-Whitney U-tests for all versions of the restricted source model RDM percents with 200 source dipoles at eccentricity 99.9 % are presented in Table 5.2.

RDM%							
	n = 1	n = 2	n = 3	n = 4	n = 5	PI	St.V.
n = 1			*	*	*		*
n = 2				*	*		*
n = 3	*					*	*
n = 4	*	*				*	*
n = 5	*	*				*	*
PI			*	*	*		*
St.V.	*	*	*	*	*	*	

Table 5.2 *The results of the Mann-Whitney U-test for restricted source models with n elements, partial integration, and St. Venant with 200 dipoles at eccentricity 99.9 %*

The asterisks in Table 5.2 stand for significant mutual differences between two source models, in respect of RDM% medians. The U-test outcome supports the results obtained from RDM% boxplots in Figure 5.3 as there is no remarkable difference between the source model with only one element and partial integration model. Again, the difference between one and two element source models is minor. What is also seen from the Table 5.2 is that the improvement in accuracy with the fourth and fifth element is statistically random, meaning that there is no advantage in adding

more elements in source configuration after including four elements. Moreover, there is a significant distinction between St. Venant and other source types.

Similar test was performed for lnMAG%, but there were no considerable differences between the source model lnMAG% medians. This validates the interpretation from Figure 5.3 that all the source models perform at the similar accuracy when it comes to magnitude aspects.

5.2 The Results of the Adaptive Version

The RDM and the lnMAG percents for the adaptive dipolar source models with $n = 1, \ldots, 6$ patch elements in source configuration with the larger testing dipole group with 100 dipoles for each eccentricity 20, 40, 60, 80, and 99.9 %, are presented in Figures 5.4 and 5.5.

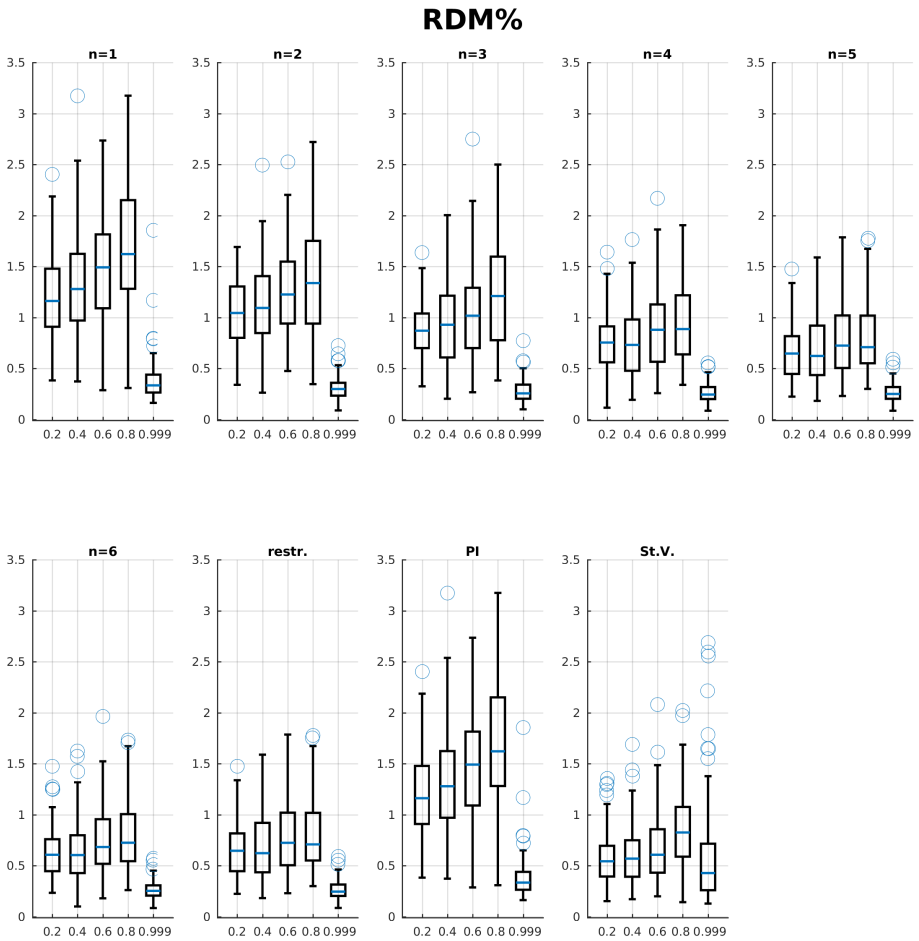

Figure 5.4 *The RDM% for the adaptive source model with n elements in source configuration with dipoles at eccentricities 20, 40, 60, 80, and 99.9 %. The results with the restricted dipolar source model, partial integration and St. Venant are also included.*

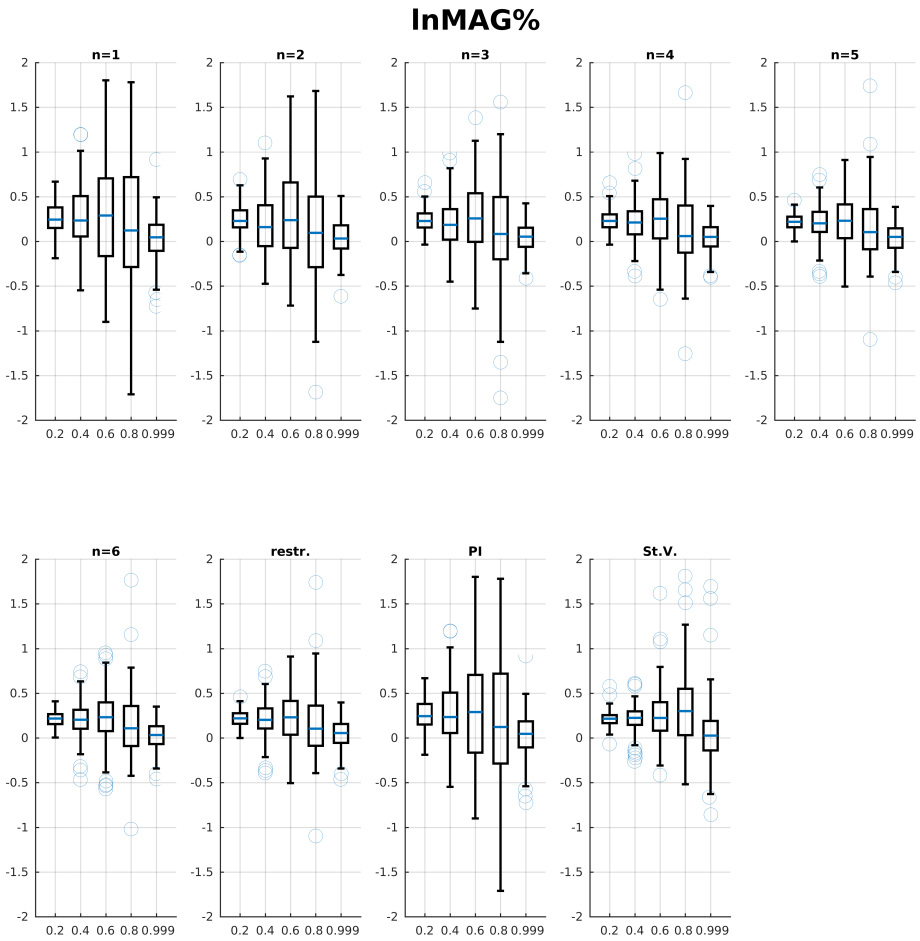

Figure 5.5 *The lnMAG% for the adaptive source model with n elements in source configuration with dipoles at eccentricities 20, 40, 60, 80, and 99.9 %. Again, the results with the restricted dipolar model, partial integration and St. Venant are also shown.*

Further, the median values of the RDM% and lnMAG% for all eccentricities are presented in Table 5.3.

The median of RDM%									
eccentricity	n = 1	n = 2	n = 3	n = 4	n = 5	n=6	restr.	PI	St.V.
20 %	1.16	1.04	0.87	0.75	0.65	0.61	0.65	1.16	0.54
40 %	1.28	1.09	0.93	0.73	0.62	0.60	0.62	1.28	0.57
60 %	1.49	1.22	1.02	0.88	0.72	0.68	0.72	1.49	0.61
80 %	1.62	1.34	1.21	0.89	0.71	0.72	0.71	1.62	0.82
99.9 %	0.33	0.30	0.25	0.24	0.25	0.25	0.24	0.33	0.43
The median of lnMAG%									
eccentricity	n = 1	n = 2	n = 3	n = 4	n = 5	n=6	restr.	PI	St.V.
20 %	0.24	0.23	0.23	0.23	0.22	0.22	0.22	0.24	0.21
40 %	0.23	0.16	0.18	0.21	0.20	0.20	0.20	0.23	0.22
60 %	0.29	0.24	0.26	0.25	0.23	0.23	0.23	0.29	0.22
80 %	0.12	0.10	0.08	0.06	0.10	0.11	0.10	0.12	0.30
99.9 %	0.05	0.03	0.05	0.05	0.05	0.03	0.05	0.05	0.03

Table 5.3 *The error medians for the adaptive source models with n elements with 100 test dipoles at each eccentricity*

The results attained with the adaptive version illustrate similar characteristics as the ones reached in the previous section with the restricted dipolar source model. St. Venant outperforms the other source models at eccentricities 0 - 60 % with lowest RDM% values (0.54 - 0.61 %). On the other hand, the difference to the adaptive dipolar source model with six patch elements is modest, highest difference between the RDM% medians is 0.10 %. Once again, the accuracy for the dipolar source model increases when there are more elements included in the patch. The adaptive version with six elements provides also slightly more accurate results than the restricted dipolar source model that has a maximum of five elements in the patch. As previously, the outcome of partial integration and dipolar source model with one element in patch have equivalent RDM% and lnMAG% errors. For the highest eccentricity, St. Venant produces the least accurate potential values, as can be seen from the error range at boxplot graph in Figure 5.4.

The RDM% and lnMAG% for adaptive type models with 200 testing dipoles at eccentricity 99.9 % are presented in Figure 5.6.

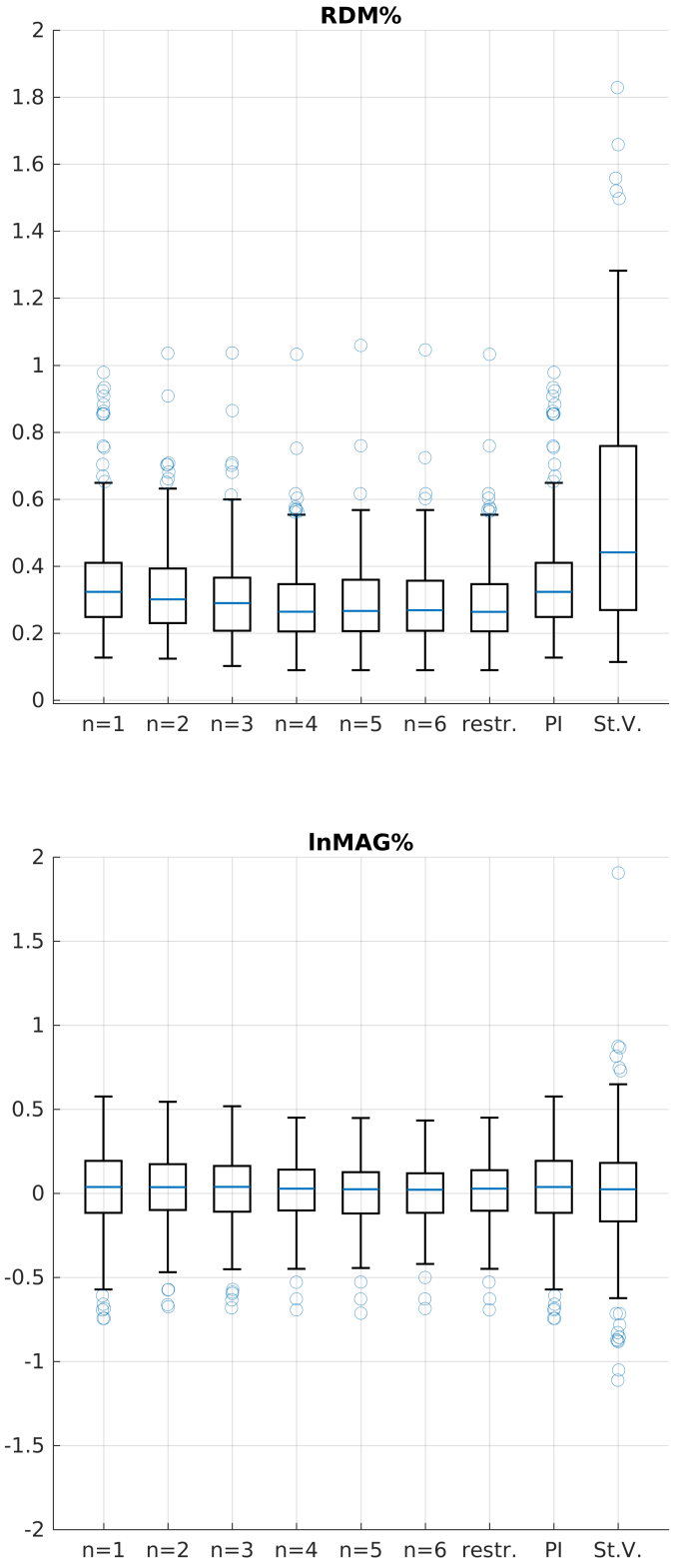

Figure 5.6 *The RDM% (upper figure) and the lnMAG% (lower figure) for the adaptive source model with n elements in source configuration, for the restricted dipolar sources, for partial integration and for St. Venant with 200 dipoles at eccentricity 99.9 %.*

As earlier, the corresponding errors for St. Venant, partial integration and the restricted version of divergence conforming source model are plotted in Figure 5.6. The restricted source model was implemented with at the maximum five source elements. Likewise for the results presented earlier with restricted dipolar source models, the element patch with only one element gives virtually the same results as partial integration. In addition, the St. Venant gives the highest RDM% error with median 0.441 %, whereas the lowest median is obtained with restricted source model (0.263%).

RDM%									
	n = 1	n = 2	n = 3	n = 4	n = 5	n=6	restr.	PI	St.V.
n = 1			*	*	*	*	*		*
n = 2				*	*	*	*		*
n = 3	*							*	*
n = 4	*	*						*	*
n = 5	*	*						*	*
n = 6	*	*						*	*
restric.	*	*						*	*
PI			*	*	*	*	*		*
St.V.	*	*	*	*	*	*	*	*	

Table 5.4 *The results of the Mann-Whitney U-test for the adaptive type source model with n elements for 200 dipoles at eccentricity 99.9 % compared to the other source types*

In the same way as in Section 5.1, the significant mutual differences between models with 200 dipoles at eccentricity 99.9 % in respect of RDM% medians are marked with asterisks in the Table 5.4. Again, all p-values in Mann-Whitney U-tests for lnMAG% medians were higher than 0.05, meaning that no significant differences between source models can be found in terms of magnitude error. Once again, there is no significant difference between the RDM percents for divergence conforming source models with one or two elements and partial integration. In the same way as with restricted version testing, the RDM % median for St. Venant differs statistically from the results of other source models. In addition, there is no remarkable statistical difference between the source models with five or six elements and the restricted version.

5.3 Discussion

As it is known from previous studies,[46] partial integration is known to act as a highly focal source method whereas St. Venant is noted as relatively accurate for forward EEG modeling. The ideal source model would be both: focal but also accurate, and the divergence conforming source types have potential for this.

Based on the results presented in Sections 5.1 and 5.2, the most accurate source model type for representing neural currents that are located at eccentricities 0-60 % is St. Venant. However, the outcome of the restricted divergence conforming source model with five elements, and similarly the results for the adaptive version with six elements were close to the St. Venant results. Vice versa, the poorest results for these locations were obtained with partial integration and the one element dipolar source model. The results for the dipolar divergence conforming source models seemed to improve as the amount of elements in source patch was increased, for both restricted and adaptive versions. Nevertheless, having more than $n = 4$ elements in the source patch does not seem to bring any advantage to the modeling accuracy. Forming the source configuration in an adaptive way did not show any significant progression compared to the restricted, previously studied version. Actually, the restricted version seemed to outperform the adaptive version at eccentricity 99.9%. This indicates that there is no potential to develop the adaptive source model further in the context of forward EEG modeling with spherical meshes.

Overall, all types of source models investigated seem to provide a high accuracy when modeling with spherical models. The RDM% in all cases was under 2 % and similarly, lnMAG errors remained under 2 %.

It should be noted that the outcome of this study is valid only with spherical models. Hence, it could be sensible to apply the adaptive version of divergence conforming source models to a realistic head model in order to see how the adaptivity suits complex, realistic structures. In addition, there could be assessed the differences between source models by taking the inverse approach. By doing this, it could be clarified a better vision which source model is the most suitable for interpreting the EEG data. Together with inverse modeling, the evaluation could be extended with real EEG measurements, providing some information whether the source models are applicable also in real-world cases.

6. CONCLUSIONS

The aim of this thesis was to study the H(div) approach for finite element method based EEG forward modeling. There were two main objectives for the thesis project: Implementation of the divergence conforming dipolar source model to an open source C++ toolbox DUNE and numerical analysis of the EEG forward modeling with H(div) approach for spherical grids. The EEG forward problem refers to a partial differential equation, whereby the aim is to estimate the potentials on the surface of the head, caused by neural activity, i.e. source currents in the human brain. With the finite element method (FEM) approach, the modeled area is discretized into a tetrahedral mesh in which each cell has an individual conductivity value.

The H(div) source models are based on the linear, zeroth order Raviart-Thomas basis functions. These functions provide a mathematically rigorous base with divergence conforming source space, and are used in this study to form face based basis functions carried in two adjacent tetrahedra. Also, the quadratic basis functions are harnessed here to model the edge based basis functions in a global mesh structure. Taking these face based and edgewise basis functions, a mathematical point-dipole is formed between either face or edge sharing nodes. As a result, there can be created different sets of source configurations where there are either only face based source dipoles, edgewise source dipoles or a mixture set from both categories. Furthermore, the amount of mesh elements can be varied as far as desired. An interpolation method called position based optimization (PBO) was applied for estimating the position and moment of a given dipole by a linear combination of source dipoles.

In this study, two approaches for dipolar divergence conforming source types were studied: previously studied, restricted version, and an adaptive one. In addition, the impact of source configuration size, i.e. the amount of patch elements, was investigated for both types. The numerical tests were analyzed with a spherical grid that had six layers, and tested with two separate sets of testing dipoles. Moreover, the computed potentials were evaluated against an analytical solution, which is known to be highly accurate with a spherical model. There were two reference methods, partial integration and St. Venant, included in the comparisons. The obtained results were analyzed with MATLAB, and the error measures used were

relative difference measure (RDM%), logarithmic magnitude error (lnMAG%) and the Mann-Whitney U-test.

As a part of this thesis project, the divergence conforming source model was implemented to an open source software called DUNE, which is a modular C++ toolbox for solving partial differential equations. [17, 15, 10, 9] In fact, the source model scripts were added to a DUNE based toolbox called duneuro, which is designed for modeling the forward EEG and MEG problems with FEM, for instance.[1, 26, 45] All the numerical tests for this thesis were accomplished with duneuro.

The main findings of the numerical analysis indicate that the H(div) - approach is a robust option for EEG source modeling. The St. Venant method resulted in lower errors than H(div)-type source model for sources that are located at eccentricities 20-60 %, but the differences in error medians were relatively small. The results for source dipoles near gray matter boundary, i.e. at eccentricity 99.9 %, suggest that H(div) - type sources are rather accurate for modeling the potentials caused by dipoles at high eccentricities. Moreover, the results obtained for divergence conforming source models with four, five and six patch elements for dipoles at high eccentricities were significantly better than the results for St. Venant or partial integration. In addition, it was obtained that the RDM % error decreased as the amount of the elements in source configuration was increased. However, for sources at high eccentricities there were no significant improvements after increasing the patch size over four elements. In addition, forming the source configuration in an adaptive way did not bring any noteworthy progress on modeling accuracy. It was also evident that the results obtained with partial integration and H(div)- source type with one patch element were identical.

Over and above, all the source types studied provided relatively accurate outcomes in all testing scenarios, as the RDM % and lnMAG % errors were in the range of 2 %. Finally, the results of this study are applicable only for forward modeling with spherical meshes that are discretized with tetrahedra. Therefore, further research with e.g. an inverse approach is required for investigating the effect of adaptivity of the source configuration and similarly, the effect of the patch element size on modeling accuracy.

BIBLIOGRAPHY

[1] "duneuro toolbox home page," retrieved 11 August, 2017. [Online]. Available: https://gitlab.dune-project.org/groups/duneuro

[2] "Niedermeyer's electroencephalography; basic principles, clinical applications, and related fields, 6th ed. (online access included)," *Reference and Research Book News*, vol. 26, no. 1, p. n/a, Feb 2011 2011. [Online]. Available: http://search.proquest.com/docview/848780007?accountid=27303

[3] "Compumedics Neuroscan, Neuroscan home page," 2017, retrieved 14 March, 2017. [Online]. Available: http://compumedicsneuroscan.com

[4] "DUNE project home page," 2017, retrieved 14 March, 2017. [Online]. Available: https://dune-project.org/

[5] M. Ainsworth and J. Coyle, "Hierarchic finite element bases on unstructured tetrahedral meshes," *International Journal for Numerical Methods in Engineering*, vol. 58, no. 14, pp. 2103–2130, 2003. [Online]. Available: http://dx.doi.org/10.1002/nme.847

[6] M. Alkåmper, A. Dedner, R. Klöfkorn, and M. Nolte, "The DUNE-ALUgrid module," *Archive of Numerical Software*, vol. 4, no. 1, 2016.

[7] Ü. Aydin, S. Rampp, C. H. Wolters, *et al.*, "Zoomed MRI guided by combined EEG/MEG source analysis: A multimodal approach for optimizing presurgical epilepsy work-up and its application in a multi-focal epilepsy patient case study," *Brain Topography*, vol. 30, no. 4, pp. 417–433, 2017. [Online]. Available: https://link.springer.com/article/10.1007/s10548-017-0568-9

[8] Ü. Aydin, J. Vorwerk, C. H. Wolters, *et al.*, "Combined EEG/MEG can outperform single modality EEG or MEG source reconstruction in presurgical epilepsy diagnosis," *PLoS ONE*, vol. 10, no. 3, 2015.

[9] P. Bastian, M. Blatt, A. Dedner, C. Engwer, *et al.*, "A generic grid interface for parallel and adaptive scientific computing. part II: Implementation and tests in DUNE," *Computing*, vol. 82, no. 2-3, pp. 121–138, 2008.

[10] P. Bastian, M. Blatt, A. Dedner, C. Engwer, K. R., *et al.*, "A generic grid interface for parallel and adaptive scientific computing. part I: Abstract framework," *Computing*, vol. 82, no. 2-3, pp. 103–119, 2008.

[11] P. Bastian, F. Heimann, and S. Marnach, "Generic implementation of finite element methods in the Distributed and Unified Numerics Environment (DUNE)," *Kybernetika*, vol. 46, no. 2, pp. 294–315, 2010. [Online]. Available: http://eudml.org/doc/197255

[12] M. Bauer, S. Pursiainen, J. Vorwerk, H. Köstler, and C. H. Wolters, "Comparison study for Whitney (Raviart-Thomas) type source models in finite element method based EEG forward modeling," *IEEE Transactions on Biomedical Engineering*, vol. 62, no. 11, pp. 2648–2656, 2015.

[13] H. Berger, "Über das Elektrenkephalogramm des Menschen," *Arch.Psychiat.Nervenkr.*, vol. 87, pp. 527–570, 1929.

[14] O. Bertrand, M. Thévenet, and F. Perrin, "3D finite element method in brain electrical activity studies," in *Biomagnetic Localization and 3D Modelling*, J. Nenonen, H. Rajala, and T. Katila, Eds. Report of the Dep. of Tech.Physics, Helsinki University of Technology, 1991, pp. 154–171.

[15] M. Blatt, A. Burchardt, A. Dedner, C. Engwer, J. Fahlke, *et al.*, "The Distributed and Unified Numerics Environment, version 2.4." *Archive of Numerical Software*, vol. 4, no. 100, pp. 13–29, 2016.

[16] M. Blatt, "A parallel algebraic multigrid method for elliptic problems with highly discontinuous coefficients," Dissertation, Heidelberg University, 2010. [Online]. Available: http://www.ub.uni-heidelberg.de/archiv/10856

[17] M. Blatt and P. Bastian, *The Iterative Solver Template Library.* Springer Berlin Heidelberg, 2007, pp. 666–675. [Online]. Available: http://dx.doi.org/10.1007/978-3-540-75755-9_82

[18] D. Braess, *Finite elements : theory, fast solvers, and applications in solid mechanics*, 2nd ed. Cambridge: Cambridge University Press, 2001.

[19] R. Brette and A. Destexhe, *Handbook of Neural Activity Measurement.* Cambridge University Press, 2012. [Online]. Available: http://www.di.ens.fr/~brette/HandbookMeasurement/

[20] H. Buchner, G. Knoll, M. Fuchs, A. Rienäcker, R. Beckmann, M. Wagner, J. Silny, and J. Pesch, "Inverse localization of electric dipole current sources in finite element models of the human head," *Electroencephalography and clinical Neurophysiology*, vol. 102, no. 4, pp. 267–278, 1997.

[21] G. Buzsáki, C. A. Anastassiou, and C. Koch, "The origin of extracellular fields and currents - EEG, ECoG, LFP and spikes," *Nature reviews. Neuroscience*,

vol. 13, no. 6, pp. 407–420, print 2012, 10.1038/nrn3241. [Online]. Available: http://dx.doi.org/10.1038/nrn3241

[22] T. R. Chandrupatla and A. D. Belegundu, *Introduction to finite elements in engineering*, 4th ed. Upper Saddle River (NJ): Prentice Hall, 2012.

[23] T. Collura, "History and evolution of electroencephalographic instruments and techniques," *Journal of clinical neurophysiology : official publication of the American Electroencephalographic Society*, vol. 10, no. 4, pp. 476–504, October 1993. [Online]. Available: http://europepmc.org/abstract/MED/8308144

[24] F. L. da Silva, "EEG and MEG: Relevance to neuroscience," *Neuron*, vol. 80, no. 5, pp. 1112 – 1128, 2013. [Online]. Available: http://www.sciencedirect.com/science/article/pii/S0896627313009203

[25] J. De Munck, C. Wolters, and M. Clerc, *EEG and MEG: forward modeling*, R. Brette and A. Destexhe, Eds. 'Handbook of Neural Activity Measurement', Cambridge University Press, 2012.

[26] C. Engwer, J. Vorwerk, J. Ludewig, and C. H. Wolters, "A discontinuous galerkin method to solve the EEG forward problem using the subtraction approach," *SIAM J. Sci. Comp.*, vol. 39, no. 1, 2017. [Online]. Available: http://epubs.siam.org/doi/abs/10.1137/15M1048392

[27] J. Fish and T. Belytschko, *A First Course in Finite Elements*. John Wiley & Sons, Ltd, 2007. [Online]. Available: http://dx.doi.org/10.1002/9780470510858.oth1

[28] D. Geselowitz, "On bioelectric potentials in an inhomogeneous volume conductor," *Biophysical Journal*, vol. 7, pp. 1–11, 1967.

[29] ——, "On the magnetic field generated outside an inhomogeneous volume conductor by internal current sources," *IEEE Transactions on Magnetics*, vol. MAG 6, pp. 346–347, 1970.

[30] B. GmbH, "BESA MRI 2.0, software web page," retrieved 11 August, 2017. [Online]. Available: http://www.besa.de/products/besa-mri/besa-mri-overview

[31] R. Grech *et al.*, "Review on solving the inverse problem in EEG source analysis," *Journal of NeuroEngineering and Rehabilitation*, vol. 5, 2008.

[32] H. Hallez, B. Vanrumste, R. Grech, J. Muscat, W. De Clercq, A. Vergult, Y. D'Asseler, K. P. Camilleri, S. G. Fabri, S. Van Huffel, and I. Lemahieu, "Review on solving the forward problem in EEG source analysis," *Journal*

of NeuroEngineering and Rehabilitation, vol. 4, no. 1, p. 46, 2007. [Online]. Available: http://dx.doi.org/10.1186/1743-0003-4-46

[33] M. Hämäläinen, R. Hari, R. J. Ilmoniemi, J. Knuutila, and O. V. Lounasmaa, "Magnetoencephalography - theory, instrumentation, and applications to noninvasive studies of the working human brain," *Reviews of Modern Physics*, vol. 65, no. 2, pp. 413–497, 1993.

[34] M. Hollander, D. A. Wolfe, and E. Chicken, *Nonparametric Statistical Methods*. Somerset: Wiley, 2013, iD: 1550549.

[35] M. B. J. Vorwerk, M. Clerc and C. Wolters, "Comparison of boundary element and finite element approaches to the EEG forward problem," *Biomedical Engineering / Biomedizinische Technik, 57(SI-1 Track-O)*, pp. 795–798, 2012. [Online]. Available: doi:10.1515/bmt-2012-4152

[36] T. Kirkman, "Statistics to use," 1996, retrieved 2 August 2017. [Online]. Available: http://www.physics.csbsju.edu/stats/

[37] S. Lew, C. H. Wolters, T. Dierkes, C. Röer, and R. S. MacLeod, "Accuracy and run-time comparison for different potential approaches and iterative solvers in finite element method based EEG source analysis," *Appl. Numer. Math.*, vol. 59, no. 8, pp. 1970–1988, Aug. 2009. [Online]. Available: http://dx.doi.org/10.1016/j.apnum.2009.02.006

[38] H. B. Mann and D. R. Whitney, "On a test of whether one of two random variables is stochastically larger than the other," *Ann. Math. Statist.*, vol. 18, no. 1, pp. 50–60, 1947. [Online]. Available: http://dx.doi.org/10.1214/aoms/1177730491

[39] MathWorks, "Statistics and machine learning toolbox: User's guide (r2017b)," Natick, Massachusetts, 2017, retrieved July 12, 2017. [Online]. Available: https://se.mathworks.com/help/stats/ranksum.html

[40] MATLAB, *version 9.1 (R2016b)*. Natick, Massachusetts: The MathWorks Inc., 2016.

[41] J. Munck and M. Peters, "A fast method to compute the potential in the multisphere model," *IEEE transactions on biomedical engineering*, vol. 40, no. 11, pp. 1166–1174, 1993.

[42] S. Murakami and Y. Okada, "Contributions of principal neocortical neurons to magnetoencephalography and electroencephalography signals," *J.Physiol.*, vol. 575, no. 3, pp. 925–936, 2006.

[43] K. Najarian and R. Splinter, *Biomedical signal and image processing.* Boca Raton: CRC |Taylor & Francis, 2006.

[44] P. L. Nunez, *Electric fields of the brain : the neurophysics of EEG.* New York: Oxford University Press, 1981.

[45] M. Piastra, A. Nüßing, J. Vorwerk, *et al.*, "The discontinuous Galerkin finite element method for solving the MEG forward problem," 2017, submitted for publication to Frontiers in Neuroscience.

[46] S. Pursiainen, J. Vorwerk, and C. Wolters, "Electroencephalography (EEG) forward modeling via H(div) finite element sources with focal interpolation," *Physics in Medicine and Biology*, vol. 61, no. 24, pp. 8502–8520, 11 2016.

[47] J. Sarvas, "Basic mathematical and electromagnetic concepts of the biomagnetic inverse problem," *Physics in Medicine and Biology*, vol. 32, no. 1, p. 11, 1987. [Online]. Available: http://stacks.iop.org/0031-9155/32/i=1/a=004

[48] L. Sörnmo and P. Laguna, *Bioelectrical signal processing in cardiac and neurological applications.* New York: Academic Press, 2005. [Online]. Available: https://tut.finna.fi/Record/tutcat.177996

[49] E.-J. Speckmann, C. E. Elger, and A. Gorji, "Neurophysiologic basis of EEG and DC potentials," 2017, retrieved 17 July, 2017. [Online]. Available: https://neupsykey.com/neurophysiologic-basis-of-eeg-and-dc-potentials

[50] J. Vorwerk, "New finite element methods to solve the EEG/MEG forward problem," Dissertation, Der Westfälischen Wilhelms-Universität Münster, 2016. [Online]. Available: http://www.sci.utah.edu/~wolters/PaperWolters/2016/Vorwerk_Dissertation_2016.pdf

[51] J. Vorwerk, J.-H. Cho, S. Rampp, H. Hamer, T. Knösche, and C. Wolters, "A guideline for head volume conductor modeling in EEG and MEG," *NeuroImage*, vol. 100, pp. 590–607, 2014.

[52] C. Wolters, L. Grasedyck, and W. Hackbusch, "Efficient computation of lead field bases and influence matrix for the FEM-based EEG and MEG inverse problem," *Inverse Problems*, vol. 20, no. 4, pp. 1099–1116, 2004. [Online]. Available: http://iopscience.iop.org/0266-5611/20/4/007/

[53] C. Wolters, H. Köstler, C. Möller, *et al.*, "Numerical mathematics of the subtraction approach for the modeling of a current dipole in EEG source reconstruction using finite element head models," *SIAM J. on*

Scientific Computing, vol. 30, no. 1, pp. 24–45, 2007. [Online]. Available: http://epubs.siam.org/doi/abs/10.1137/060659053

[54] C. Wolters, M. Kuhn, A. Anwander, and S. Reitzinger, "A parallel algebraic multigrid solver for finite element method based source localization in the human brain," *Computing and Visualization in Science*, vol. 5, no. 3, pp. 165–177, 2002.

[55] Y. Yan, P. Nunez, and R. Hart, "Finite-element model of the human head: scalp potentials due to dipole sources," *Medical and Biological Engineering and Computing*, vol. 29, no. 5, pp. 475–481, 1991.

[56] Y. Zhang, Z. Ren, and D. Lautru, "Finite element modeling of current dipoles using direct and subtraction methods for EEG forward problem," *COMPEL - The international journal for computation and mathematics in electrical and electronic engineering*, vol. 33, no. 1/2, pp. 210–223, 2013. [Online]. Available: https://doi.org/10.1108/COMPEL-11-2012-0329

APPENDIX A. AN EXAMPLE OF A DUNEURO SCRIPT IN MATLAB INTERFACE

```
%%create driver object
cfg = [];
cfg.type = 'fitted';
cfg.element_type = 'tetrahedron';
cfg.solver_type = 'cg';

load GridDataForTesting.mat
cfg.volume_conductor.grid.nodes = nodes;
cfg.volume_conductor.grid.elements = elements;
cfg.volume_conductor.tensors.labels = labels;
cfg.volume_conductor.tensors.conductivities = conductivities
    ;
driver = duneuro_meeg(cfg);

clear nodes elements labels

%% read dipoles
load TestingDipoles.mat
dipoles = [dipole_positions;dipole_directions];
clear dipole_positions dipole_directions

%% set electrodes
cfg = [];
cfg.type = 'normal'; %projection to mesh surface
driver.set_electrodes(electrodes, cfg);

%% compute transfer matrix
cfg = [];
cfg.solver.reduction = '1e-10';
transfer_matrix = driver.compute_eeg_transfer_matrix(cfg);

%% potentials for restricted dipolar source model
lead_field_w_regular= zeros(size(electrodes, 2), size(
    dipoles,2));

```

```
34 cfg = [];
35 cfg.type = 'whitney';
36 cfg.restricted = 'true';
37 cfg.referenceLength = '20';
38 cfg.faceSources = 'all';
39 cfg.edgeSources = 'all';
40 cfg.n_ele = '4';
41 cfg.interpolation = 'PBO';
42 driver.set_source_model(cfg);
43
44 cfg = [];
45 cfg.post_process = 'true';
46 cfg.subtract_mean = 'true';
47 for i=1:size(dipoles, 2)
48     lead_field_w_regular(:,i) = driver.apply_eeg_transfer(
       transfer_matrix, dipoles(:,i), cfg);
49 end
50
51 %% potentials for adaptive dipolar source model wtih pbo,
   one element in patch
52 lead_field_w_pbo_1= zeros(size(electrodes, 2), size(dipoles
   ,2));
53
54 cfg = [];
55 cfg.type = 'whitney_newapproach';
56 cfg.restricted = 'true';
57 cfg.referenceLength = '20';
58 cfg.upbound = '78.01';
59 cfg.tolerance = '1.e-6';
60 cfg.plot = 'false';
61 cfg.elements = '0';
62 cfg.interpolation = 'PBO';
63 driver.set_source_model(cfg);
64
65 cfg = [];
66 cfg.post_process = 'true';
67 cfg.subtract_mean = 'true';
68 for i=1:size(dipoles, 2)
69     lead_field_w_pbo_0(:,i) = driver.apply_eeg_transfer(
```

```
        transfer_matrix, dipoles(:,i), cfg);
end

%% similarly for element patches with n=2,...,5 elements
....

%% Compute potentials for partial integration
lead_field_p= zeros(size(electrodes, 2), size(dipoles,2));

cfg = [];
cfg.type = 'partial_integration';
driver.set_source_model(cfg);

cfg = [];
cfg.post_process = 'true';
cfg.subtract_mean = 'true';
for i=1:size(dipoles, 2)
    lead_field_p(:,i) = driver.apply_eeg_transfer(
        transfer_matrix, dipoles(:,i), cfg);
end

%% Compute potentials for St. Venant
lead_field_v= zeros(size(electrodes, 2), size(dipoles,2));

cfg = [];
cfg.type = 'venant';
cfg.relaxationFactor = '1e-8';
cfg.weightingExponent = '1';
cfg.restrict = 'true';
cfg.initialization = 'closest_vertex';
cfg.numberOfMoments = '3';
cfg.referenceLength = '20';
driver.set_source_model(cfg);

cfg = [];
cfg.post_process = 'true';
cfg.subtract_mean = 'true';
for i=1:size(dipoles, 2)
    lead_field_v(:,i) = driver.apply_eeg_transfer(
```

```
        transfer_matrix, dipoles(:,i), cfg);
107
108 end
109
110 %% compute analytical solution
111 analytical = zeros(size(electrodes, 2), size(dipoles, 2));
112 cfg = [];
113 cfg.radii = '92 86 80 78';
114 cfg.conductivities = '0.00033 0.0000042 0.00179 0.00033';
115 cfg.center = '0 0 0';
116
117 for i = 1:size(dipoles, 2)
118     analytical(:,i) = duneuro_matlab('
        eeg_analytical_solution', cfg, electrodes, dipoles(:,
        i));
119 end
120
121 %% compute source statistics
122 eccentricities = round(sqrt(sum((dipoles(1:3,:)-0).^2,1))
    /78,3);
123
124 lf_norm_w_regular = sqrt(sum(lead_field_w_regular.^2,1));
125 ...
126
127 mag_w_regular = 100*(lf_norm_w_regular./an_norm-1);
128 ...
129
130
131 rdm_w_regular = 50*sqrt(sum((lead_field_w_regular./...
132                             (ones(size(lead_field_w_regular,1)
                                ,1)*lf_norm_w_regular)...
133                             -analytical./(ones(size(analytical
                                ,1),1),1)*...
134                                         an_norm)).^2,1));
135 ...
136
137 %% Mann - Whitney U-tests for RDM% and lnMAG%'s
138 P0(1,1) = ranksum(rdm_w_pbo_1, rdm_w_pbo_1);
139 P0(1,2) = ranksum(rdm_w_pbo_1, rdm_w_pbo_2);
```

```
140 ...
141
142
143 % Write a txt-file of Mann-Whitney results
144 names = {'n=1', 'n=2',...
145           'n=3', 'n=4', 'n=5','n=6','reg W', 'PI', 'SV'};
146
147 output_file = './results/adaptiveapproach_mwu.txt';
148 fid = fopen(output_file, 'w+');
149 fprintf(fid, '%4s\n', 'RDM%');
150 fprintf(fid, '%12s %8s %8s %8s %8s %9s %8s %8s %9s\n', 'n=1'
    , 'n=2',...
151           'n=3', 'n=4', 'n=5','n=6', 'reg W', 'PI', 'SV');
152
153 for ii=1:numel(names)
154           fprintf(fid, '%5s %8.4f %8.4f %8.4f %8.4f %8.4f
              %8.4f %8.4f %9.4f %8.4f\n',...
155                   names{ii},P0(1,ii),P1(1,ii),P2(1,ii),P3(1,
                      ii),...
156                   P4(1,ii),P5(1,ii),PREG(1,ii),PP(1,ii),PS(1,
                      ii));
157 end
158 fprintf(fid,'\n');
159 fprintf(fid, '%4s\n', 'lnMAG%');
160 fprintf(fid, '%12s %8s %8s %8s %8s %9s %8s %8s %9s\n', 'n=1'
    , 'n=2',...
161           'n=3', 'n=4', 'n=5','n=6','reg W', 'PI', 'SV');
162
163 for ii=1:numel(names)
164           fprintf(fid, '%5s %8.4f %8.4f %8.4f %8.4f %8.4f
              %8.4f %8.4f %9.4f %8.4f\n',...
165                   names{ii},P0(2,ii),P1(2,ii),P2(2,ii),P3(2,
                      ii),...
166                   P4(2,ii),P5(2,ii),PREG(2,ii),PP(2,ii),PS
                      (2,ii));
167 end
168 fclose(fid);
169
170 %% Plot RDM and lnMAG statistics
```

```
171
172 import iosr.statistics.*
173 y_reg = tab2box(eccentricities, rdm_w_regular);
174 y_w_1 = tab2box(eccentricities, rdm_w_pbo_1);
175 ...
176
177 y2_reg = tab2box(eccentricities, mag_w_regular);
178 y2_w_1 = tab2box(eccentricities, mag_w_pbo_1);
179
180 import iosr.statistics.*
181
182 ylimm = 2;
183 figure('position',[0,0,500,500])
184 bp = boxPlot({'n=1','n=2','n=3','n=4','n=5', 'n=6','restr.',
    'PI','St.V.'},...
185                [y_w_1,y_w_2,y_w_3,y_w_4,y_w_5,y_w_6,y_reg,y_p,
                      y_v],...
186                'Notch',false,'Limit','1.5IQR');
187 ylim([-0.01 ylimm])
188 grid();
189 title('RDM%')
190 imtit = 'rdm_newapproach_varying_patchsize_200dipoles.png';
191 print(imtit, '-dpng', '-r400')
192
193 ylimm = 2;
194 figure('position',[0,0,500,500])
195 bp = boxPlot({'n=1','n=2','n=3','n=4','n=5','n=6','restr.','
    PI','St.V.'},...
196                [y2_w_1,y2_w_2,y2_w_3,y2_w_4,y2_w_5,y2_w_6,
                      y2_reg,y2_p,y2_v],...
197                'Notch',false,'Limit','1.5IQR');
198 ylim([-ylimm ylimm])
199 grid()
200 title('lnMAG%')
201 imtit = 'mag_newapproach_varying_patchsize_200dipoles.png';
202 print(imtit, '-dpng', '-r400')
```